Available online at www.sciencedirect.com
SCIENCE DIRECT®
Journal of Computational Physics 213 (2006) 86–116
JOURNAL OF COMPUTATIONAL PHYSICS
www.elsevier.com/locate/jcp

Coupled atomistic–continuum simulations using arbitrary overlapping domains

P.A. Klein, J.A. Zimmerman *

Science-Based Materials Modeling Department, Sandia National Laboratories, 7011 East Avenue, Mail Stop 9042, Livermore, CA 94551, USA

Received 20 September 2004; received in revised form 9 May 2005; accepted 3 August 2005
Available online 28 September 2005

Abstract

We present a formulation for coupling atomistic and continuum simulation methods for application to both quasistatic and dynamic analyses. In our formulation, a coarse-scale continuum discretization is assumed to cover all parts of the computational domain with atomistic crystals introduced only in regions of interest. The geometry of the discretization and crystal are allowed to overlap arbitrarily. Our approach uses interpolation and projection operators to link the kinematics of each region, which are then used to formulate a system potential energy from which we derive coupled expressions for the forces acting in each region. A hyperelastic constitutive formulation is used to compute the stress response of the defect-free continuum with constitutive properties derived from the Cauchy–Born rule. A correction to the Cauchy–Born rule is introduced in the overlap region to minimize fictitious boundary effects. Features of our approach will be demonstrated with simulations in one, two and three dimensions.

Keywords: Atomistic simulation; Continuum mechanics; Coupling; Finite elements

1. Introduction

A primary objective of modern materials modeling is to predict the material response and failure governed by deformation mechanisms, and to assess the mechanical reliability of components. These material deformation mechanisms operate at specific length scales, which vary from nanometers to microns. Multi-scale materials simulations have been the focus of many studies [1] using techniques such as atomistic simulation, phase-field calculations, and finite element (FE) analysis. Continuum mechanical modeling efforts have evolved beyond using ad hoc failure criteria to include cohesive approaches for surface separation and damage accumulation models for bulk material degradation. However, these techniques only capture anticipated deformation phenomena. Atomistic simulation procedures, such as molecular statics (MS) and dynamics (MD), use simple interatomic potentials as the underlying constitutive relation between material particles and allow the derived

* Corresponding author. Tel.: +1 925 2942437; fax: +1 925 2941459.
E-mail addresses: pklein@frk.com (P.A. Klein), jzimmer@sandia.gov (J.A. Zimmerman).

0021-9991/$ - see front matter
doi:10.1016/j.jcp.2005.08.014

forces to govern the basic physics of the system's response to an applied load. These potentials use parameters fitted from ab initio calculations and physical measurements of material properties. Atomistic simulation operates at the length scale of interatomic separation, and has the ability to display competing mechanisms of material deformation, such as fracture, dislocation nucleation and propagation, and void nucleation, growth and coalescence. However, limits of computational power prohibits analysis of micro-scale systems using only atomistic simulation, even in large-scale, parallel calculations.

It is clear that some coupled methodology must be established to combine the strengths of both atomistic and continuum modeling. Although this field has acquired a substantial history, it remains an active area of research. Among the many challenges with developing coupled approaches, the main issue is eliminating fictitious boundary effects. For dynamic problems, this issue typically involves avoiding spurious wave reflections, while for quasistatic problems, the issue is fictitious forces. The appearance of fictitious forces in coupled atomistic–continuum systems stems from an inconsistency in the formulation of the potential energy and is therefore an issue for dynamic analysis as well, though it tends to be treated as secondary to or completely overlooked compared with the wave reflection issue within the dynamic context. As one might expect, the issue of fictitious forces is not limited to coupled atomistic–continuum formulations and indeed has been studied within the context of multiscale continuum methods by Fish and Yuan [2], arising as one attempts to reconcile the coarse and fine scale representations of the solution.

In early work by Kohlhoff and collaborators [3,4], they developed a methodology that combined finite element analysis with atomistic modeling, named FEAt. The FEAt model uses an atomic lattice surrounded by an FE mesh with a limited overlap region that enforces boundary conditions on both atomistic and continuum domains. Consistency is achieved by requiring the strains in the overlap region to be equal for both the atoms and the continuum, and by matching the elastic properties of the continuum constitutive model to those derived from the governing interatomic potential. In [4], non-linear elasticity is used via a Taylor series expansion of elastic energy about strain that contains first, second and third order elastic constants. The FEAt model works well for static simulations, but displays some anomalous behavior for dynamics. However, it has the inherent disadvantage that the FE mesh within the overlap region must be refined so that nodal spacing is at the atomic scale with nodal positions dictated by the crystal lattice structure.

More recently, several methods have been introduced that attempt to improve upon the original efforts by Kohlhoff et al. These include the Quasicontinuum (QC) method by Tadmor et al. [5], coarse-grained molecular dynamics (CGMD) by Rudd and Broughton [6], molecular-atomistic-ab initio dynamics (MAAD) by Broughton et al. [7], and the bridging scale decomposition (BSD) by Wagner and Liu [8]. The QC method uses an FE representation of the displacement field over the entire domain, requiring mesh refinement to the atomic scale in regions of severe deformation. The strain energy within an element is determined from a single ''representative atom'' embedded in a locally constructed crystallite. At lower levels of deformation, elements may be much larger than the atomistic length scale, and the lattice is assumed to deform homogeneously as described by the continuum deformation gradient. Deformation of increasing severity triggers mesh refinement until the element size is reduced to the atomic scale. Under these conditions, the local crystallite spans multiple elements, leading to a non-local calculation of the strain energy. Consistency between refined and coarse areas is achieved by using finite deformation elasticity [9] and the Cauchy–Born rule [10,11] that equates interatomic bond energy to continuum potential energy in order to develop a non-linear continuum constitutive model based on the interatomic potential used for atomistic simulation. While the QC approach allows a blending between atomistic and continuum regions, it possess the disadvantages of a reliance on adaptive mesh refinement to the atomic scale, a computationally intensive task, and an inability to eliminate fictitious boundary effects at the local/non-local boundary.

Coarse-grained molecular dynamics consists of replacing the underlying atomic lattice with nodes representing either individual atoms or a weighted average collection of atoms. The total energy of the system is calculated from the potential and kinetic energies of the nodes plus a thermal energy term for the missing degrees of freedom assumed to be at a uniform temperature. CGMD produces phonon spectra with wavelength dependencies similar to those for pure atomistics; however, CGMD does possess wavelength-dependent limitations on energy transmission. Newer versions of CGMD include implementation of a generalized Langevin equation (GLE) to dissipate high frequency motions not representable in the coarser-scaled regions [12] and development of CGMD is ongoing.

More similar to Kohlhoff et al.'s methodology, the MAAD approach separates the physical system into distinct MD and FE regions. The system's total Hamiltonian consists of contributions from each individual region as well as a contribution from ''hand-shaking'' between regions. The FE mesh in this hand-shaking zone is refined to the atomic scale and nodes occupy positions that atoms would occupy if the atomic region was extended into the FE domain. Kinetic energy is attributed to both nodes and atoms in the hand-shaking zone, while away from this zone uniform temperature terms are added to account for the missing degrees of freedom, just as for CGMD. MAAD has successfully exhibited smooth and non-reflective transmission of elastic waves between MD and FE regions, but it does suffer from the same limitations as CGMD. At the hand-shaking zone, kinetic motion of atoms is transferred into dynamic motion of nodes. While this allows temperature to be represented as motion in the continuum region, nodes, unlike atoms, have no physical meaning and are introduced only as part of the numerical discretization. The solution should be independent of nodal positions, which is certainly not the case for atomistic simulation and atomic positions.

Most recently, Wagner and Liu [8] have developed the bridging scale decomposition approach for application to both static and dynamic atomistic–continuum coupling. Their approach uses a continuous FE mesh for the entire domain with smaller regions of atoms placed in regions where high fidelity modeling is needed. Atomistic simulation, either MS or MD, is performed in the usual manner and the FE displacement solution for the overlying mesh is determined from projection of the atomic displacements using FE shape functions. This projection is known as the ''bridging scale''; it is the portion of the atomistic simulation solution that must be subtracted from the total in order to separate the displacements into a coarse scale, resolvable onto the FE mesh, and a fine scale. For the FE domain that does not contain underlying atoms, the FE solution is solved in the usual manner. Coupling between the two regions is accomplished by the expressions for forces on atoms and nodes and by using ''ghost'' atoms that interact with free atoms at the atomic-FE boundary and whose displacements are determined by interpolation of the FE displacement field. For dynamic problems, Wagner and Liu have minimized reflections at the atomic-FE boundary by using GLE's to account for the effect of the missing fine scale degrees of freedom in the isolated FE mesh. Park et al. have extended the BSD method to two- [13] and three- [14] dimensional systems by numerically computing the resulting impedance force that needs to be eliminated in order to represent the missing fine scale degrees of freedom. They have used this extension to simulate elastic wave propagation and dynamic crack growth. The BSD approach possesses many advantages; however, neither [8] nor [13,14] specify how to partition potential energy consistently in the overlapping elements that are defined by both free and projected nodes and contain bonds between free and ghost atoms. This partitioning is the crucial factor in minimizing fictitious forces within the overlap region, as will be shown.

The coupling methods listed above have been used successfully to simulate materials deformation such as crack-grain boundary interactions, dislocation nucleation from nanoindentation and the dynamic fracture of silicon. However, the weaknesses of these methods show that more consideration is needed in developing a coupled atomistic–continuum approach. Specifically, methods such as FEAt, MAAD and BSD do not provide a rigorous basis for how to partition potential energy between atomistic bonds and continuum strain energy within the overlap regions. The MAAD methodology overlaps atomistics and continuum within an extremely small region, and arbitrarily combines $\frac{1}{2}$ of the energy from the atomic bonds and $\frac{1}{2}$ of the continuum strain energy to arrive at the full Hamiltonian for the coupled system. For the BSD approach, the overlap region is wider and uses the mechanism of ghost atoms; however, ghosts are introduced in an ad hoc manner and the existence of ghosts is not included in the equilibrium equations. In addition, the authors do not specify either how to count bonds between free and ghost atoms or how the density of such bonds should contribute to the strain energy within overlapping elements. The problem of proper partitioning of potential energy terms has largely been overlooked, and is often simplified in many overlaying grid methodologies such as the bridging domain method by Xiao and Belytschko [15]. In that article, the authors analyze coupling for a one-dimensional chain and used a simple ratio of distance from a point to the boundary of the continuum region over the total projected length of the atomic-continuum overlap region to scale the atomistic and continuum contributions to the system energy from material within the overlap region. It was found that this simple ratio is insufficient to eliminate spurious wave reflection in two-dimensional systems, and was then modified in an ad hoc manner.

As already mentioned, the improper partitioning of system potential energy leads to fictitious forces acting on atoms and nodes within the overlap region. These forces are often referred to as "ghost forces" and have been a subject focused upon for continued development in atomistic–continuum coupling methods. For instance, the recent review article by Curtin and Miller [16] details the origins and effects of ghost forces that arise due to use of the QC method. They also revisit an approach by Shenoy et al. [17] to determine corrections that can be introduced to the QC methodology to compensate for ghost forces. This approach involves the use of dead loads equal and opposite to the ghost forces determined from the undeformed configuration of the system. While the introduction of this correction is noteworthy, it inevitably leads to inaccuracies once the crystal is deformed, even for homogeneous loading conditions, or if the lattice is subject to any rotation. Also discussed in Curtin and Miller's article is the development by Knap and Ortiz [18] of a fully non-local formulation of the QC method. This approach bypasses the use of the Cauchy–Born rule and instead determines nodal forces by constructing a small cluster of representative atoms surrounding a node and calculating the force using the non-local, atomistic description. From the description of this method in [16], it seems that nodes are chosen from an underlying atomic lattice and that nodal positions coincide with a subset of atomic positions for a given configuration (nodes are, in fact, referred to as representative atoms). The nodal forces are weighted to account for the degree of coarsening of the nodal density with respect to the atomic density of the underlying lattice. This coarsening in regions of high nodal density is the only source of error for this method, although the computational cost is high compared with methods that use the Cauchy–Born rule and may not be warranted for systems with slowly varying deformation gradients.

In all, these efforts confirm that the issue of how to partition energy within an atomistic–continuum overlap regions needs to be addressed properly in order to maintain the integrity of the two views of material deformation, atomistic and continuum, and to obtain accurate solutions. Our goal for this work is to develop a formulation that preserves the integrity of the MS and FE methods for separate regions, but adapt each method to partition potential energy consistently in the overlap region.

In this paper, we describe the formulation and implementation of a method to compute the potential energy of a coupled atomistic–continuum system that has application to both quasistatic and dynamic analyses. As with the other overlapping domain methods described above, the approach employs a finite element formulation covering all parts of the computational domain to solve the coarse scale displacements, while subregions of interest are also covered with an atomistic crystal to resolve the fine scale displacements. The kinematics of the coupling between the coarse and fine scale fields, through project and interpolation operators, are explicitly included in the statement of the system potential energy which then naturally gives rise to coupled expressions for the forces acting at each scale. The kinematics of the coupling are described in detail in Section 2. The resulting force equilibrium equation are developed in Section 3. In Section 4, a local rather than global projection operator is introduced for improved computational efficiency. An inevitable consequence of the overlapping domain formulation is the question of how each scale contributes to the potential energy around the edges of the atomistic regions. As mentioned above, inconsistencies in this partitioning give rise fictitious forces. Away from edges of the atomistic regions, the potential energy is computed entirely from continuum and atomistic contributions in the FE and atomistic regions, respectively.

The coupling approach proposed here to address the fictitious forces requires that a constitutive model based on the Cauchy–Born rule is used to define the stress response of the continuum. These models directly incorporate the lattice structure and interatomic potentials of the atomistic description allowing them to reproduce exactly the response of an infinite, defect-free crystal subject to finite, homogeneous deformations. These constitutive models are readily constructed for centrosymmetric lattices with pair potentials, and can also be extended to more complex crystal structures than cannot be described by a simple Bravais lattice with a single atom per unit cell. The extension of the Cauchy–Born assumption to complex lattices was outlined some time ago by Stakgold [19]. Tadmor et al. [20] present a general formulation of Stakgold's approach to finite crystal elasticity with specific application to the diamond cubic lattice, while Huang et al. [21] apply the approach to develop continuum constitutive models for graphene sheets and nanotubes. A continuum description based on the Cauchy–Born rule is needed because spatially varying bond densities are introduced in these models which are then solved to determine the partition of the system potential energy consistently at the edges of the atomistic regions. Consistency is defined by directly minimizing fictitious forces. Force rather than energy is used to define consistency because the energy density is ambiguously defined for the atomistic

system at the edges of the crystal. Guided by the concept of a "patch test" [22], the consistency condition is solved for the system under conditions of homogeneous deformation. If consistency can be achieved for this case, it implies the solution can be systematically improved by either refining the mesh or moving the interface between the atomistic and continuum regions farther away from the areas of inhomogeneous deformation. As will be demonstrated, the solution of the consistency condition does not assume linearity in the response of the atomistic system or infinitesimal strains in the continuum. Once solved, the densities are carried by the continuum, maintaining consistency for all homogeneous finite strains and rotations. Explicit expressions for the fictitious forces arising in the coupled system and our approach for minimizing them are described in Section 5. The approach of finding consistency between the coarse and fine scale descriptions by introducing a spatially varying bond densities in the continuum is applicable to all crystals that can be described by the Cauchy–Born assumption. However, the development in Section 5 demonstrates how the approach is applied specifically to centrosymmetric crystals with pair potentials. Application of the approach to other interatomic potentials and lattice types will be the focus of future work.

The goal of employing formal projection and interpolation operators to link the coarse and fine scale fields, combined with the direct minimization of fictitious forces, is to allow the crystal and mesh to overlap arbitrarily. By arbitrary, we mean no special correspondence is required between the location of the atoms or termination of crystals and the positions of the nodes or element boundaries in the finite element mesh. These characteristics are highlighted in the examples presented in Sections 7.1–7.3. Indeed, the approach does not require a regular mesh, or nodes arranged in lattice-like configurations. The approach does not need to be reformulated for application to different element topologies, as we demonstrate with quadrilateral and hexahedral elements, as well as triangular and tetrahedral elements which allow greater flexibility in mesh generation. Crystals can be located anywhere within the domain and at any orientation. Also, no restrictions are made about the configuration of the interface. It is not limited to planar configurations and may be applied to interfaces with edges and corners, as demonstrated in the examples, or general undulations without modification. Though not investigated in this work, the method would allow adaptivity of the crystal, for tracking defects, without requiring changes to the mesh.

The approach is not limited to single crystal orientations. Polycrystals can be treated by defining different crystal orientations across the domain. With a standard finite element formulation, there would be restrictions on how grain boundaries could intersect the atomistic–continuum interface. Standard finite element representations of the displacement field can only reproduce the sharp strain discontinuities associated with grain boundaries at element boundaries. Similarly, the current formulation is limited to defect-free crystals at the atomistic–continuum interface, and defects such as dislocations cannot pass from the crystal into the continuum. A primary reason for this shortcoming is that methods for representing these defects within a finite deformation continuum setting are not well-developed, nor is it clear how one would calculate the constitutive response of the defected material. Extending the coupling approach to handle interactions between defects and the atomistic–continuum interface is rich area beyond the scope of this work.

2. Kinematics of quasistatic coupling

Consider a coupled atomistic–continuum system as shown in Fig. 1. It is assumed that a finite element mesh covers all parts of the computational domain, while only limited regions of interest are also covered with an atomic crystal. For example, such a region may be the volume of material immediately surrounding a crack tip, or the material at the free surface of a solid that will be mechanically loaded by a nanoindenter. Let the atomistic displacements in the system be written as

$$\breve{\mathbf{Q}} = [\mathbf{q}^{(\alpha)}, \mathbf{q}^{(\beta)}, \ldots, \mathbf{q}^{(\gamma)}]^{\mathrm{T}}, \quad \alpha, \beta, \ldots, \gamma \in \breve{\mathscr{A}}, \tag{1}$$

where $\mathbf{q}^{(\alpha)}$ is the displacement of atom (α) and $\breve{\mathscr{A}}$ is the set of all atoms. Likewise, let the nodal displacements be written as

$$\breve{\mathbf{U}} = [\mathbf{u}^{(a)}, \mathbf{u}^{(b)}, \ldots, \mathbf{u}^{(c)}]^{\mathrm{T}}, \quad a, b, \ldots, c \in \breve{\mathscr{N}}, \tag{2}$$

where $\mathbf{u}^{(a)}$ is the displacement of node (a) and $\breve{\mathscr{N}}$ is the set of all finite element nodes. In this paper, lower case Greek symbols are used for atom indices, while lower case Roman symbols are used for node indices. In order

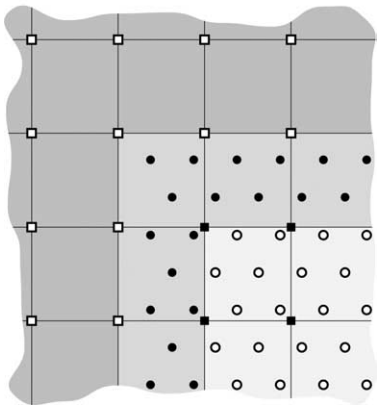

Fig. 1. Patch of a coupled atomistic–continuum system. The set of finite element nodes $\mathscr{N}$ is shown as □. The set of nodes $\hat{\mathscr{N}}$ is shown as ■. The set of atoms $\mathscr{A}$ is shown as ○, and the set of atoms $\hat{\mathscr{A}}$ is shown as ●.

to satisfy boundary conditions for both regions, the motion of some of the atoms is prescribed by the continuum displacement field. This subset of atomistic displacements is denoted by

$$\hat{\mathbf{Q}} = [\mathbf{q}^{(\alpha)}, \mathbf{q}^{(\beta)}, \ldots, \mathbf{q}^{(\gamma)}]^{\mathrm{T}}, \quad \alpha, \beta, \ldots, \gamma \in \hat{\mathscr{A}}, \tag{3}$$

while the complement which contains the unprescribed atomistic displacements is denoted by

$$\mathbf{Q} = [\mathbf{q}^{(\delta)}, \mathbf{q}^{(\epsilon)}, \ldots, \mathbf{q}^{(\eta)}]^{\mathrm{T}}, \quad \delta, \epsilon, \ldots, \eta \in \mathscr{A}, \tag{4}$$

where

$$\hat{\mathscr{A}} \cup \mathscr{A} = \breve{\mathscr{A}} \quad \text{and} \quad \hat{\mathscr{A}} \cap \mathscr{A} = \emptyset. \tag{5}$$

Similar to the BSD approach found in [8], atoms that belong to the set $\hat{\mathscr{A}}$ are referred to as ghost atoms, while atoms that belong to the set $\mathscr{A}$ are referred to as free atoms. Analogously, the motion of some finite element nodes is prescribed by the underlying lattice. These displacements are denoted by

$$\hat{\mathbf{U}} = [\mathbf{u}^{(a)}, \mathbf{u}^{(b)}, \ldots, \mathbf{u}^{(c)}]^{\mathrm{T}}, \quad a, b, \ldots, c \in \hat{\mathscr{N}}, \tag{6}$$

while the unprescribed nodal displacements are denoted by

$$\mathbf{U} = [\mathbf{u}^{(m)}, \mathbf{u}^{(n)}, \ldots, \mathbf{u}^{(s)}]^{\mathrm{T}}, \quad m, n, \ldots, s \in \mathscr{N}, \tag{7}$$

where likewise

$$\hat{\mathscr{N}} \cup \mathscr{N} = \breve{\mathscr{N}} \quad \text{and} \quad \hat{\mathscr{N}} \cap \mathscr{N} = \emptyset. \tag{8}$$

One can interpolate the continuum displacement field to the location of any atom as

$$\mathbf{u}(\mathbf{X}^{(\alpha)}) = \sum_{a \in \breve{\mathscr{N}}} N^{(a)}(\mathbf{X}^{(\alpha)})\mathbf{u}^{(a)}, \tag{9}$$

where $\mathbf{X}^{(\alpha)}$ is the undeformed position of atom (α) and $N^{(a)}$ is the shape function associated with node (a). The nodal shape functions typically have compact support, so the sum in (9) involves only the nodes whose support includes $\mathbf{X}^{(\alpha)}$. Generally, one can consider the atomistic and continuum displacement fields to be related as

$$\begin{Bmatrix} \mathbf{Q} \\ \hat{\mathbf{Q}} \end{Bmatrix} = \mathbf{N} \begin{Bmatrix} \mathbf{U} \\ \hat{\mathbf{U}} \end{Bmatrix} + \begin{Bmatrix} \mathbf{Q}' \\ 0 \end{Bmatrix}, \tag{10}$$

where

$$\mathbf{N} = \begin{bmatrix} \mathbf{N}_{\mathbf{Q}\mathbf{U}} & \mathbf{N}_{\mathbf{Q}\hat{\mathbf{U}}} \\ \mathbf{N}_{\hat{\mathbf{Q}}\mathbf{U}} & \mathbf{N}_{\hat{\mathbf{Q}}\hat{\mathbf{U}}} \end{bmatrix}. \tag{11}$$

The sub-matrices of $\mathbf{N}$ contain shape functions as defined by the interpolation given in (9). The component of the atomistic displacements,

$$\mathbf{Q}' = [\mathbf{q}'^{(\alpha)}, \mathbf{q}'^{(\beta)}, \ldots, \mathbf{q}'^{(\gamma)}]^{\mathrm{T}}, \quad \alpha \in \mathscr{A}, \tag{12}$$

where $\mathbf{q}'^{(\alpha)} = \mathbf{q}^{(\alpha)} - \bar{\mathbf{q}}^{(\alpha)}$ for $\alpha \in \mathscr{A}$ and

$$\bar{\mathbf{q}}^{(\alpha)} = \sum_{a \in \check{\mathscr{N}}} N^{(a)}(\mathbf{X}^{(\alpha)})\mathbf{u}^{(a)}, \quad \alpha \in \mathscr{A}, \tag{13}$$

is introduced since the finite element shape functions in $\mathbf{N}_{\mathbf{QU}}$ and $\mathbf{N}_{\mathbf{Q}\hat{\mathbf{U}}}$ are generally too coarse to represent the atomistic displacements exactly. It will be the convention in this paper to display the portion of any quantity $\mathbf{S}$ that can be represented at a coarse scale using the finite element shape functions with the overbar symbol, $\bar{\mathbf{S}}$, while any portion of $\mathbf{S}$ that cannot be represented by the finite element shape functions is deemed "fine scale" and is displayed using the accent symbol, $\mathbf{S}'$. This is similar to the convention used in [8]. Indeed, much of the kinematic description presented thus far closely resembles the BSD methodology as given in [8]. However, in this work the symbols $\mathbf{Q}$ and $\mathbf{q}$ strictly refer to the displacements of atoms and the symbol $\mathbf{U}$ only refers to the displacements of finite element nodes. The symbol $\mathbf{u}$ refers to the continuum displacement field as dictated by the finite element solution. It can be evaluated at points that coincide with atoms $\mathbf{u}(\mathbf{X}^{(\alpha)})$, nodes $\mathbf{u}^{(a)}$, or any point contained within the finite element mesh $\mathbf{u}(\mathbf{X})$.

Since $\mathbf{Q}$ and $\hat{\mathbf{U}}$ may have arbitrary dimensions, where we expect the number of atoms represented in $\mathbf{Q}$ to be larger than the number of finite elements nodes represented in $\hat{\mathbf{U}}$, $\mathbf{N}^{-1}_{\mathbf{Q}\hat{\mathbf{U}}}$ will not be defined, and so the prescribed nodal displacements $\hat{\mathbf{U}}$ are chosen to minimize the error

$$e = \mathbf{Q}' \cdot \mathbf{Q}' = \sum_{\alpha \in \mathscr{A}} \left[\mathbf{q}^{(\alpha)} - \sum_{a \in \check{\mathscr{N}}} N^{(a)}(\mathbf{X}^{(\alpha)})\mathbf{u}^{(a)} \right]^2. \tag{14}$$

The nodal displacements $\mathbf{u}^{(a)}$ for $a \in \hat{\mathscr{N}}$ are determined by solving

$$\sum_{\alpha \in \mathscr{A}} \mathbf{q}^{(\alpha)} N^{(b)}(\mathbf{X}^{(\alpha)}) - \sum_{\alpha \in \mathscr{A}} \sum_{c \in \mathscr{N}} N^{(c)}(\mathbf{X}^{(\alpha)})\mathbf{u}^{(c)} N^{(b)}(\mathbf{X}^{(\alpha)}) = \sum_{\alpha \in \mathscr{A}} \sum_{a \in \hat{\mathscr{N}}} N^{(a)}(\mathbf{X}^{(\alpha)})\mathbf{u}^{(a)} N^{(b)}(\mathbf{X}^{(\alpha)}), \quad b \in \hat{\mathscr{N}}, \tag{15}$$

which is the discretized L_2 projection of the atomistic displacements onto the finite element space containing $N^{(a)}$ for $a \in \hat{\mathscr{N}}$ using the atomistic positions $\mathbf{X}^{(\alpha)}$ for $\alpha \in \mathscr{A}$ as integration points. In this work, the fine scale part of atomistic displacements $\mathbf{Q}'$ is used only as an error estimation, and can be used to guide the addition or removal of atoms from the crystal. In the work of Wagner and Liu [8], this fine scale part is used in conjunction with a bridging scale formulation to develop a method for dynamic coupling.

The solution to (15) can be expressed in matrix notation by first rewriting (14) as

$$e = [\mathbf{Q} - \mathbf{N}_{\mathbf{QU}}\mathbf{U} - \mathbf{N}_{\mathbf{Q}\hat{\mathbf{U}}}\hat{\mathbf{U}}] \cdot [\mathbf{Q} - \mathbf{N}_{\mathbf{QU}}\mathbf{U} - \mathbf{N}_{\mathbf{Q}\hat{\mathbf{U}}}\hat{\mathbf{U}}], \tag{16}$$

which is minimized for

$$\hat{\mathbf{U}} = \mathbf{M}^{-1}_{\hat{\mathbf{U}}\hat{\mathbf{U}}}[\mathbf{N}^{\mathrm{T}}_{\mathbf{Q}\hat{\mathbf{U}}}\mathbf{Q} - \mathbf{N}^{\mathrm{T}}_{\mathbf{Q}\hat{\mathbf{U}}}\mathbf{N}_{\mathbf{QU}}\mathbf{U}], \tag{17}$$

where

$$\mathbf{M}_{\hat{\mathbf{U}}\hat{\mathbf{U}}} = \mathbf{N}^{\mathrm{T}}_{\mathbf{Q}\hat{\mathbf{U}}}\mathbf{N}_{\mathbf{Q}\hat{\mathbf{U}}}. \tag{18}$$

The development of this projection from the fine, atomic scale to a coarser scale was first presented in [6] for CGMD, and has also been used in a similar fashion for the BSD approach [8]. However, the presence of the second term on the right-hand side of Eq. (17) is innovative from these previous efforts by allowing the possibility that elements containing both free and ghost atoms may be bounded by both prescribed and free nodes. For this situation, the existence of interpolation functions connecting free atoms and nodes, $\mathbf{N}_{\mathbf{QU}}$, is necessary. From (10) and (17), we can express the prescribed atomistic displacements entirely in terms of the free atomistic and nodal displacements as

$$\hat{\mathbf{Q}} = [\mathbf{N}_{\hat{\mathbf{Q}}\mathbf{U}} - \mathbf{N}_{\hat{\mathbf{Q}}\hat{\mathbf{U}}}\mathbf{M}^{-1}_{\hat{\mathbf{U}}\hat{\mathbf{U}}}\mathbf{N}^{\mathrm{T}}_{\mathbf{Q}\hat{\mathbf{U}}}\mathbf{N}_{\mathbf{QU}}]\mathbf{U} + \mathbf{N}_{\hat{\mathbf{Q}}\hat{\mathbf{U}}}\mathbf{M}^{-1}_{\hat{\mathbf{U}}\hat{\mathbf{U}}}\mathbf{N}^{\mathrm{T}}_{\mathbf{Q}\hat{\mathbf{U}}}\mathbf{Q}, \tag{19}$$

which shows the prescribed atomistic displacements depend not only on the displacements of the free finite element nodes, but also on the displacements of the free atoms through the projection of those displacements onto the overlapping part of the finite element mesh.

Note that $\mathbf{M}_{\hat{\mathcal{U}}\hat{\mathcal{U}}}$ has the structure (although not the dimensional units) of the finite element mass matrix, evaluated using the atomistic coordinates as integration points. Immediately, we recognize that this matrix will be rank deficient if an insufficient number of atoms lie in the support of every node $a \in \hat{\mathcal{N}}$. This number of atoms will depend on the element topology. One can propose conditions for the stability of the projection. First, it is necessary there be at least as many atoms in $\mathcal{A}$ as there are nodes in $\hat{\mathcal{N}}$; however, this is not sufficient to insure the stability of the projection. The number of atoms in the supports of the nodes in $\hat{\mathcal{N}}$ can be considered on an element-by-element basis. For instance, the mass matrix for a bilinear quad requires four integration points to avoid rank deficiency, a sufficient but not necessary condition to avoid rank deficiency of the assembled matrix. Combined, the necessary and sufficient conditions ensure the stability of the projection. The cost of the projection can be reduced by using a diagonal, or "lumped", approximation to the mass matrix. With this projection matrix, the nodal displacements will not be optimal for minimizing the error (14), so less of the atomistic displacement information will be transferred to the nodes and more will remain as error. Moreover, the lumped approximation does not allow linearly varying fields to be projected exactly, a condition that will be required in the subsequent formulation.

We can simplify Eqs. (17) and (19) into the forms

$$\hat{\mathbf{U}} = \mathbf{B}_{\hat{\mathcal{U}}\mathcal{Q}}\mathbf{Q} + \mathbf{B}_{\hat{\mathcal{U}}\mathcal{U}}\mathbf{U}, \tag{20}$$

$$\hat{\mathbf{Q}} = \mathbf{B}_{\hat{\mathcal{Q}}\mathcal{Q}}\mathbf{Q} + \mathbf{B}_{\hat{\mathcal{Q}}\mathcal{U}}\mathbf{U}, \tag{21}$$

respectively, where

$$\mathbf{B}_{\hat{\mathcal{U}}\mathcal{Q}} = \mathbf{M}^{-1}_{\hat{\mathcal{U}}\hat{\mathcal{U}}}\mathbf{N}^{\mathrm{T}}_{\mathcal{Q}\hat{\mathcal{U}}}, \tag{22}$$

$$\mathbf{B}_{\hat{\mathcal{U}}\mathcal{U}} = -\mathbf{M}^{-1}_{\hat{\mathcal{U}}\hat{\mathcal{U}}}\mathbf{N}^{\mathrm{T}}_{\mathcal{Q}\hat{\mathcal{U}}}\mathbf{N}_{\mathcal{Q}\mathcal{U}} = -\mathbf{B}_{\hat{\mathcal{U}}\mathcal{Q}}\mathbf{N}_{\mathcal{Q}\mathcal{U}}, \tag{23}$$

$$\mathbf{B}_{\hat{\mathcal{Q}}\mathcal{Q}} = \mathbf{N}_{\hat{\mathcal{Q}}\hat{\mathcal{U}}}\mathbf{M}^{-1}_{\hat{\mathcal{U}}\hat{\mathcal{U}}}\mathbf{N}^{\mathrm{T}}_{\mathcal{Q}\hat{\mathcal{U}}} = \mathbf{N}_{\hat{\mathcal{Q}}\hat{\mathcal{U}}}\mathbf{B}_{\hat{\mathcal{U}}\mathcal{Q}}, \tag{24}$$

$$\mathbf{B}_{\hat{\mathcal{Q}}\mathcal{U}} = \mathbf{N}_{\hat{\mathcal{Q}}\mathcal{U}} - \mathbf{N}_{\hat{\mathcal{Q}}\hat{\mathcal{U}}}\mathbf{M}^{-1}_{\hat{\mathcal{U}}\hat{\mathcal{U}}}\mathbf{N}^{\mathrm{T}}_{\mathcal{Q}\hat{\mathcal{U}}}\mathbf{N}_{\mathcal{Q}\mathcal{U}} = \mathbf{N}_{\hat{\mathcal{Q}}\mathcal{U}} - \mathbf{B}_{\hat{\mathcal{Q}}\mathcal{Q}}\mathbf{N}_{\mathcal{Q}\mathcal{U}}. \tag{25}$$

This simplified nomenclature will produce cleaner and more easily understood equilibrium equations in the next section.

3. Coupled equilibrium equations

Eqs. (20) and (21) provide us the means to express the displacements of both projected nodes $\hat{\mathbf{U}}$ and interpolated atoms $\hat{\mathbf{Q}}$ as functions of the unprescribed atomic $\mathbf{Q}$ and nodal $\mathbf{U}$ displacements. To solve for these unprescribed displacements, we must develop equilibrium equations that are derived by formulating the total potential energy of the entire coupled atomistic–continuum systems. We express the potential energy of the coupled system as

$$\Pi(\mathbf{Q},\mathbf{U}) = \Pi_{\mathbf{Q}} + \Pi_{\mathbf{U}} - \mathbf{F}_{\mathbf{Q}}\cdot\mathbf{Q} - \mathbf{F}_{\mathbf{U}}\cdot\mathbf{U}, \tag{26}$$

where $\Pi_{\mathbf{Q}}$ represents the potential energy in the bonds of the crystal, $\Pi_{\mathbf{U}}$ is the strain energy density integrated over the continuum, and $\mathbf{F}_{\mathbf{Q}}$ and $\mathbf{F}_{\mathbf{U}}$ are external forces acting on the atoms and finite element nodes, respectively. To include the structure of the coupling between the atomistic and continuum displacement fields from (20) and (21), we rewrite the contributions to the total potential as

$$\Pi_{\mathbf{Q}} = \Pi_{\mathbf{Q}}(\mathbf{Q},\mathbf{U}) = \Pi_{\mathbf{Q}}(\mathbf{Q},\hat{\mathbf{Q}}(\mathbf{Q},\mathbf{U})), \tag{27}$$

$$\Pi_{\mathbf{U}} = \Pi_{\mathbf{U}}(\mathbf{Q},\mathbf{U}) = \Pi_{\mathbf{U}}(\mathbf{U},\hat{\mathbf{U}}(\mathbf{Q},\mathbf{U})). \tag{28}$$

Incorporating the coupling relationships directly in the total potential insures that the coupled system will also remain conservative if a hyperelastic formulation is used for calculating the continuum response. The equations of static equilibrium are derived from total potential as

$$\mathbf{R}_{\mathbf{Q}} = \frac{\partial \Pi}{\partial \mathbf{Q}} = \frac{\partial \Pi_{\mathbf{Q}}}{\partial \mathbf{Q}} + \frac{\partial \Pi_{\mathbf{Q}}}{\partial \hat{\mathbf{Q}}}\frac{\partial \hat{\mathbf{Q}}}{\partial \mathbf{Q}} + \frac{\partial \Pi_{\mathbf{U}}}{\partial \hat{\mathbf{U}}}\frac{\partial \hat{\mathbf{U}}}{\partial \mathbf{Q}} - \mathbf{F}_{\mathbf{Q}} = 0, \tag{29}$$

$$\mathbf{R}_{\mathbf{U}} = \frac{\partial \Pi}{\partial \mathbf{U}} = \frac{\partial \Pi_{\mathbf{U}}}{\partial \mathbf{U}} + \frac{\partial \Pi_{\mathbf{U}}}{\partial \hat{\mathbf{U}}}\frac{\partial \hat{\mathbf{U}}}{\partial \mathbf{U}} + \frac{\partial \Pi_{\mathbf{Q}}}{\partial \hat{\mathbf{Q}}}\frac{\partial \hat{\mathbf{Q}}}{\partial \mathbf{U}} - \mathbf{F}_{\mathbf{U}} = 0. \tag{30}$$

Using (20) and (21), the equilibrium equations can be expressed as

$$\mathbf{R}_{\mathbf{Q}} = \frac{\partial \Pi_{\mathbf{Q}}}{\partial \mathbf{Q}} + \mathbf{B}^{\mathrm{T}}_{\hat{\mathbf{Q}}\mathbf{Q}}\frac{\partial \Pi_{\mathbf{Q}}}{\partial \hat{\mathbf{Q}}} + \mathbf{B}^{\mathrm{T}}_{\hat{\mathbf{U}}\mathbf{Q}}\frac{\partial \Pi_{\mathbf{U}}}{\partial \hat{\mathbf{U}}} - \mathbf{F}_{\mathbf{Q}} = 0, \tag{31}$$

$$\mathbf{R}_{\mathbf{U}} = \frac{\partial \Pi_{\mathbf{U}}}{\partial \mathbf{U}} + \mathbf{B}^{\mathrm{T}}_{\hat{\mathbf{U}}\mathbf{U}}\frac{\partial \Pi_{\mathbf{U}}}{\partial \hat{\mathbf{U}}} + \mathbf{B}^{\mathrm{T}}_{\hat{\mathbf{Q}}\mathbf{U}}\frac{\partial \Pi_{\mathbf{Q}}}{\partial \hat{\mathbf{Q}}} - \mathbf{F}_{\mathbf{U}} = 0. \tag{32}$$

Linearizing the equilibrium equations about the $\mathbf{Q}$ and $\mathbf{U}$ yields

$$\mathbf{R}_{\mathbf{Q}}(\mathbf{Q},\mathbf{U}) + \frac{\partial \mathbf{R}_{\mathbf{Q}}}{\partial \mathbf{Q}}\delta\mathbf{Q} + \frac{\partial \mathbf{R}_{\mathbf{Q}}}{\partial \mathbf{U}}\delta\mathbf{U} = 0, \tag{33}$$

$$\mathbf{R}_{\mathbf{U}}(\mathbf{Q},\mathbf{U}) + \frac{\partial \mathbf{R}_{\mathbf{U}}}{\partial \mathbf{Q}}\delta\mathbf{Q} + \frac{\partial \mathbf{R}_{\mathbf{U}}}{\partial \mathbf{U}}\delta\mathbf{U} = 0, \tag{34}$$

which may be written in matrix form as

$$\begin{bmatrix} \mathbf{K}_{\mathbf{QQ}} & \mathbf{K}_{\mathbf{QU}} \\ \mathbf{K}_{\mathbf{UQ}} & \mathbf{K}_{\mathbf{UU}} \end{bmatrix} \begin{Bmatrix} \delta\mathbf{Q} \\ \delta\mathbf{U} \end{Bmatrix} = -\begin{Bmatrix} \mathbf{R}_{\mathbf{Q}} \\ \mathbf{R}_{\mathbf{U}} \end{Bmatrix}, \tag{35}$$

where the components of the symmetric tangent matrix are

$$\mathbf{K}_{\mathbf{QQ}} = \frac{\partial^2 \Pi_{\mathbf{Q}}}{\partial \mathbf{Q}\,\partial \mathbf{Q}} + \mathbf{B}^{\mathrm{T}}_{\hat{\mathbf{Q}}\mathbf{Q}}\frac{\partial^2 \Pi_{\mathbf{Q}}}{\partial \hat{\mathbf{Q}}\,\partial \mathbf{Q}} + \frac{\partial^2 \Pi_{\mathbf{Q}}}{\partial \mathbf{Q}\,\partial \hat{\mathbf{Q}}}\mathbf{B}_{\hat{\mathbf{Q}}\mathbf{Q}} + \mathbf{B}^{\mathrm{T}}_{\hat{\mathbf{Q}}\mathbf{Q}}\frac{\partial^2 \Pi_{\mathbf{Q}}}{\partial \hat{\mathbf{Q}}\,\partial \hat{\mathbf{Q}}}\mathbf{B}_{\hat{\mathbf{Q}}\mathbf{Q}} + \mathbf{B}^{\mathrm{T}}_{\hat{\mathbf{U}}\mathbf{Q}}\frac{\partial^2 \Pi_{\mathbf{U}}}{\partial \hat{\mathbf{U}}\,\partial \hat{\mathbf{U}}}\mathbf{B}_{\hat{\mathbf{U}}\mathbf{Q}}, \tag{36}$$

$$\mathbf{K}_{\mathbf{QU}} = \mathbf{K}^{\mathrm{T}}_{\mathbf{UQ}} = \frac{\partial^2 \Pi_{\mathbf{Q}}}{\partial \mathbf{Q}\,\partial \hat{\mathbf{Q}}}\mathbf{B}_{\hat{\mathbf{Q}}\mathbf{U}} + \mathbf{B}^{\mathrm{T}}_{\hat{\mathbf{Q}}\mathbf{Q}}\frac{\partial^2 \Pi_{\mathbf{Q}}}{\partial \hat{\mathbf{Q}}\,\partial \hat{\mathbf{Q}}}\mathbf{B}_{\hat{\mathbf{Q}}\mathbf{U}} + \mathbf{B}^{\mathrm{T}}_{\hat{\mathbf{U}}\mathbf{Q}}\frac{\partial^2 \Pi_{\mathbf{U}}}{\partial \hat{\mathbf{U}}\,\partial \mathbf{U}} + \mathbf{B}^{\mathrm{T}}_{\hat{\mathbf{U}}\mathbf{Q}}\frac{\partial^2 \Pi_{\mathbf{U}}}{\partial \hat{\mathbf{U}}\,\partial \hat{\mathbf{U}}}\mathbf{B}_{\hat{\mathbf{U}}\mathbf{U}}, \tag{37}$$

$$\mathbf{K}_{\mathbf{UU}} = \frac{\partial^2 \Pi_{\mathbf{U}}}{\partial \mathbf{U}\,\partial \mathbf{U}} + \mathbf{B}^{\mathrm{T}}_{\hat{\mathbf{U}}\mathbf{U}}\frac{\partial^2 \Pi_{\mathbf{U}}}{\partial \hat{\mathbf{U}}\,\partial \mathbf{U}} + \frac{\partial^2 \Pi_{\mathbf{U}}}{\partial \mathbf{U}\,\partial \hat{\mathbf{U}}}\mathbf{B}_{\hat{\mathbf{U}}\mathbf{U}} + \mathbf{B}^{\mathrm{T}}_{\hat{\mathbf{U}}\mathbf{U}}\frac{\partial^2 \Pi_{\mathbf{U}}}{\partial \hat{\mathbf{U}}\,\partial \hat{\mathbf{U}}}\mathbf{B}_{\hat{\mathbf{U}}\mathbf{U}} + \mathbf{B}^{\mathrm{T}}_{\hat{\mathbf{Q}}\mathbf{U}}\frac{\partial^2 \Pi_{\mathbf{Q}}}{\partial \hat{\mathbf{Q}}\,\partial \hat{\mathbf{Q}}}\mathbf{B}_{\hat{\mathbf{Q}}\mathbf{U}}. \tag{38}$$

One could use this tangent matrix within a Newton solution scheme to derive the general procedure for solving the coupled system of equations. Alternatively, we used a preconditioned conjugate gradient algorithm [23] to solve Eqs. (31) and (32) for the analyses presented in this paper.

4. Projection using moving least squares

One of the principal drawbacks with the L_2 projection is calculation of $\mathbf{M}^{-1}_{\hat{\mathbf{U}}\hat{\mathbf{U}}}$, which is required to evaluate the $\mathbf{B}$ matrices for use in either directly solving Eqs. (31) and (32) or in determining the components of the tangent matrix. An approximation to $\mathbf{M}^{-1}_{\hat{\mathbf{U}}\hat{\mathbf{U}}}$ can be used for the tangent stiffness, but approximations to the linear solution (31) required for evaluation of the residual will directly affect the accuracy of the solution. Evaluation of $\mathbf{M}^{-1}_{\hat{\mathbf{U}}\hat{\mathbf{U}}}$ becomes especially problematic with the application of the coupling scheme to dynamic problems when the residual will need to be evaluated a very large number of times.

The discretized L_2 projection (15) is not the only option for transferring the atomistic displacements to the finite element nodes. Rather than employing a global least squares approach, we can make use of a local, or so-called moving least squares (MLS), method to project atomistic information to the finite element nodes. The basis functions developed for the reproducing kernel particle method (RKPM) [24] possess a number of properties that make them well-suited for use in a coupling scheme. Among these properties are that the functions can be constructed to reproduce any desired function exactly. In particular, we will show that the basis functions must be able to reproduce a linear displacement field exactly in order for the coupled method to solve homogeneous deformations exactly. A number of additional useful properties of the basis functions is derived from the connection between RKPM and wavelets. This connection lends the interpretation of interpolating

displacements from the atoms to the finite element nodes as a low pass filtering operation with a well-characterized spectral behavior. Moreover, the wavelet formalism furnishes a method wherein a series of these filters can be constructed to produce a hierarchical decomposition of the atomistic field into components possessing different scales of information.

RKPM belongs to a class of methods for which the approximation, or "image", of a signal is given by a kernel expression. In the transfer of displacements from the atoms to the nodes, the atomic information serves as the signal while the nodal information is the image. Without loss of generality, we can consider the expression for the approximation in one dimension

$$u^{R_\varepsilon}(x) = \int_{-\infty}^{+\infty} \phi_\varepsilon(x-y)u(y)\,\mathrm{d}y, \tag{39}$$

where ϕ_ε is alternately called a weight, kernel, or smoothing function. From the analogy to signal processing, ϕ_ε may be viewed as a customizable low pass filter between the original signal, or data, $u(y)$ and its reproduced image. This function is positive, even, and has compact support characterized by the dilation parameter ε. Liu and Chen [25] improved the accuracy of the method by modifying the window function with a correction to yield a reproducing condition as

$$u^{R_\varepsilon}(x) = \int_{-\infty}^{+\infty} \bar{\phi}_\varepsilon(x-y)u(y)\,\mathrm{d}y, \tag{40}$$

where the modified window function

$$\bar{\phi}_\varepsilon(x-y) = C(x;x-y)\phi_\varepsilon(x-y) \tag{41}$$

incorporates the polynomial

$$C(x;x-y) = b_0(x) + b_1(x)(x-y) + b_2(x)(x-y)^2 + \cdots + b_m(x)(x-y)^m \tag{42}$$

which ensures that the approximation can exactly represent polynomials of order m. In general, we may express the correction function as

$$C(\mathbf{x};\mathbf{x}-\mathbf{y}) = \mathbf{b}(\mathbf{x})\cdot\mathbb{P}(\mathbf{x}-\mathbf{y}), \tag{43}$$

where $\mathbb{P}$ is a basis of polynomials that possess the desired degree of completeness and $\mathbf{b}(\mathbf{x})$ is an vector of unknown coefficients determined from the reproducing condition (40). The requirement that each member of the basis be reproduced follows from (40) as

$$\mathbb{P}(\mathbf{0}) = \int_{-\infty}^{+\infty} \mathbf{b}(\mathbf{x})\cdot\mathbb{P}(\mathbf{x}-\mathbf{y})\phi_\varepsilon(\mathbf{x}-\mathbf{y})\mathbb{P}(\mathbf{x}-\mathbf{y})\,\mathrm{d}\mathbf{y}. \tag{44}$$

The vector of coefficients follows as

$$\mathbf{b}(\mathbf{x}) = \mathbb{M}_\varepsilon^{-1}(\mathbf{x})\mathbb{P}(\mathbf{0}), \tag{45}$$

where

$$\mathbb{M}_\varepsilon(\mathbf{x}) = \int_{-\infty}^{+\infty} \mathbb{P}(\mathbf{x}-\mathbf{y})\otimes\mathbb{P}(\mathbf{x}-\mathbf{y})\phi_\varepsilon(\mathbf{x}-\mathbf{y})\,\mathrm{d}\mathbf{y} \tag{46}$$

is known as the moment matrix. $\mathbb{M}$ in the local, moving least squares method is the analog of $\mathbf{M}_{\hat{\mathcal{U}}\hat{\mathcal{U}}}$ for the global projection. However, while the dimension of $\mathbf{M}_{\hat{\mathcal{U}}\hat{\mathcal{U}}}$ is the number of projected nodes in $\hat{\mathcal{N}}$, the dimension of $\mathbb{M}$ is determined by the number of terms in the correction function (43) and is independent of the number of projected nodes. One typically enforces the reproducing condition only through linear functions, needed to represent constant strain fields, meaning $\mathbb{M}$ is 4×4 in three-dimensions. Using the result from (45), the reproducing condition (40) can be written as

$$\mathbf{u}^{R_\varepsilon}(\mathbf{x}) = \int_{-\infty}^{+\infty} \mathbf{b}(\mathbf{x})\cdot\mathbb{P}(\mathbf{x}-\mathbf{y})\phi_\varepsilon(\mathbf{x}-\mathbf{y})\mathbf{u}(\mathbf{y})\,\mathrm{d}\mathbf{y}. \tag{47}$$

In evaluating the representations for the nodal field from the atomistic information, we discretize the integrals in the previous expressions. The discrete reproducing condition follows from (47) as

$$\mathbf{u}(\mathbf{X}) = \sum_{\beta=1}^{N_p} \mathbf{b}(\mathbf{X}) \cdot \mathbb{P}(\mathbf{X} - \mathbf{X}^{(\beta)}) \phi_\varepsilon(\mathbf{X} - \mathbf{X}^{(\beta)}) \mathbf{q}^{(\beta)} \Delta V^{(\beta)}, \tag{48}$$

where N_p is the number of sampling atoms under consideration, and $\mathbf{X}^{(\beta)}$ and $\Delta V^{(\beta)}$ are the coordinates and integration weight (volume) associated with atom β, respectively. From (48), we can identify the RKPM nodal shape functions as

$$\mathbf{u}^{(a)} = \sum_{\beta=1}^{N_p} \tilde{N}^{(\beta)}(\mathbf{X}^{(a)}) \mathbf{q}^{(\beta)}, \tag{49}$$

where

$$\tilde{N}^{(\beta)}(\mathbf{X}) = \mathbf{b}(\mathbf{X}) \cdot \mathbb{P}(\mathbf{X} - \mathbf{X}^{(\beta)}) \phi_\varepsilon(\mathbf{X} - \mathbf{X}^{(\beta)}) \Delta V^{(\beta)}, \tag{50}$$

$a \in \hat{\mathscr{N}}$ and $\beta \in \mathscr{A}$.

These relations enable us to replace the term $\mathbf{M}^{-1}_{\hat{\mathbf{U}}\hat{\mathbf{U}}}\mathbf{N}^{\mathbf{T}}_{\mathbf{Q}\hat{\mathbf{U}}}$ found in Eqs. (22)–(25) with the matrix of RKPM shape functions $\tilde{\mathbf{N}}_{\hat{\mathbf{U}}\mathbf{Q}}$ defined in Eq. (50). The prescribed continuum and atomic displacements are now expressed as

$$\hat{\mathbf{U}} = \tilde{\mathbf{B}}_{\hat{\mathbf{U}}\mathbf{Q}}\mathbf{Q} + \tilde{\mathbf{B}}_{\hat{\mathbf{U}}\mathbf{U}}\mathbf{U}, \tag{51}$$

$$\hat{\mathbf{Q}} = \tilde{\mathbf{B}}_{\hat{\mathbf{Q}}\mathbf{Q}}\mathbf{Q} + \tilde{\mathbf{B}}_{\hat{\mathbf{Q}}\mathbf{U}}\mathbf{U}, \tag{52}$$

where

$$\tilde{\mathbf{B}}_{\hat{\mathbf{U}}\mathbf{Q}} = \tilde{\mathbf{N}}_{\hat{\mathbf{U}}\mathbf{Q}}, \tag{53}$$

$$\tilde{\mathbf{B}}_{\hat{\mathbf{U}}\mathbf{U}} = -\tilde{\mathbf{N}}_{\hat{\mathbf{U}}\mathbf{Q}}\mathbf{N}_{\mathbf{Q}\mathbf{U}}, \tag{54}$$

$$\tilde{\mathbf{B}}_{\hat{\mathbf{Q}}\mathbf{Q}} = \mathbf{N}_{\hat{\mathbf{Q}}\hat{\mathbf{U}}}\tilde{\mathbf{N}}_{\hat{\mathbf{U}}\mathbf{Q}}, \tag{55}$$

$$\tilde{\mathbf{B}}_{\hat{\mathbf{Q}}\mathbf{U}} = \mathbf{N}_{\hat{\mathbf{Q}}\mathbf{U}} - \mathbf{N}_{\hat{\mathbf{Q}}\hat{\mathbf{U}}}\tilde{\mathbf{N}}_{\hat{\mathbf{U}}\mathbf{Q}}\mathbf{N}_{\mathbf{Q}\mathbf{U}}. \tag{56}$$

We note that depending on the properties of the shape functions used to construct $\tilde{\mathbf{N}}_{\hat{\mathbf{U}}\mathbf{Q}}$, the coefficients of the kinematic coupling relations (53)–(56) can be reduced. $\tilde{\mathbf{N}}_{\hat{\mathbf{U}}\mathbf{Q}}$ projects the values of a function evaluated at atoms in $\mathscr{A}$ to the nodes in $\hat{\mathscr{N}}$. Similarly, (54) first evaluates a function in the space of the shape functions from nodes in $\mathscr{N}$ at atoms in $\mathscr{A}$ through $\mathbf{N}_{\mathbf{Q}\mathbf{U}}$ and then projects those values to the nodes in $\hat{\mathscr{N}}$. If the meshless shape functions are constructed to reproduce functions in the space of the nodal shape functions associated with $\mathscr{N}$ exactly, then $\tilde{\mathbf{B}}_{\hat{\mathbf{U}}\mathbf{U}} = 0$ if the nodal shape functions display the Kronecker delta property

$$N^{(a)}(\mathbf{X}^{(b)}) = \delta_{ab} \tag{57}$$

for all nodes $a, b \in \breve{\mathscr{N}}$. As a result, (56) would reduce to $\tilde{\mathbf{B}}_{\hat{\mathbf{Q}}\mathbf{U}} = \mathbf{N}_{\hat{\mathbf{Q}}\mathbf{U}}$. This simplification is not possible with the L_2 projection because the operator $\mathbf{M}^{-1}_{\hat{\mathbf{U}}\hat{\mathbf{U}}}\mathbf{N}^{\mathbf{T}}_{\mathbf{Q}\hat{\mathbf{U}}}$ can only reproduce functions in the space of the nodal shape functions associated with $\hat{\mathscr{N}}$ exactly.

Using (51) and (52), the equilibrium equations can be expressed as

$$\mathbf{R}_{\mathbf{Q}} = \frac{\partial \Pi_{\mathbf{Q}}}{\partial \mathbf{Q}} + \tilde{\mathbf{B}}^{\mathrm{T}}_{\hat{\mathbf{Q}}\mathbf{Q}} \frac{\partial \Pi_{\mathbf{Q}}}{\partial \hat{\mathbf{Q}}} + \tilde{\mathbf{B}}^{\mathrm{T}}_{\hat{\mathbf{U}}\mathbf{Q}} \frac{\partial \Pi_{\mathbf{U}}}{\partial \hat{\mathbf{U}}} - \mathbf{F}_{\mathbf{Q}} = 0, \tag{58}$$

$$\mathbf{R}_{\mathbf{U}} = \frac{\partial \Pi_{\mathbf{U}}}{\partial \mathbf{U}} + \tilde{\mathbf{B}}^{\mathrm{T}}_{\hat{\mathbf{U}}\mathbf{U}} \frac{\partial \Pi_{\mathbf{U}}}{\partial \hat{\mathbf{U}}} + \tilde{\mathbf{B}}^{\mathrm{T}}_{\hat{\mathbf{Q}}\mathbf{U}} \frac{\partial \Pi_{\mathbf{Q}}}{\partial \hat{\mathbf{Q}}} - \mathbf{F}_{\mathbf{U}} = 0, \tag{59}$$

which yield the components of the tangent matrix

$$\mathbf{K}_{\mathbf{QQ}} = \frac{\partial^2 \Pi_{\mathbf{Q}}}{\partial \mathbf{Q}\, \partial \mathbf{Q}} + \tilde{\mathbf{B}}^{\mathrm{T}}_{\hat{\mathbf{Q}}\mathbf{Q}} \frac{\partial^2 \Pi_{\mathbf{Q}}}{\partial \hat{\mathbf{Q}}\, \partial \mathbf{Q}} + \frac{\partial^2 \Pi_{\mathbf{Q}}}{\partial \mathbf{Q}\, \partial \hat{\mathbf{Q}}} \tilde{\mathbf{B}}_{\hat{\mathbf{Q}}\mathbf{Q}} + \tilde{\mathbf{B}}^{\mathrm{T}}_{\hat{\mathbf{Q}}\mathbf{Q}} \frac{\partial^2 \Pi_{\mathbf{Q}}}{\partial \hat{\mathbf{Q}}\, \partial \hat{\mathbf{Q}}} \tilde{\mathbf{B}}_{\hat{\mathbf{Q}}\mathbf{Q}} + \tilde{\mathbf{B}}^{\mathrm{T}}_{\hat{\mathbf{U}}\mathbf{Q}} \frac{\partial^2 \Pi_{\mathbf{U}}}{\partial \hat{\mathbf{U}}\, \partial \hat{\mathbf{U}}} \tilde{\mathbf{B}}_{\hat{\mathbf{U}}\mathbf{Q}}, \tag{60}$$

$$\mathbf{K}_{\mathbf{QU}} = \mathbf{K}^{\mathrm{T}}_{\mathbf{UQ}} = \frac{\partial^2 \Pi_{\mathbf{Q}}}{\partial \mathbf{Q}\, \partial \hat{\mathbf{Q}}} \tilde{\mathbf{B}}_{\hat{\mathbf{Q}}\mathbf{U}} + \tilde{\mathbf{B}}^{\mathrm{T}}_{\hat{\mathbf{Q}}\mathbf{Q}} \frac{\partial^2 \Pi_{\mathbf{Q}}}{\partial \hat{\mathbf{Q}}\, \partial \hat{\mathbf{Q}}} \tilde{\mathbf{B}}_{\hat{\mathbf{Q}}\mathbf{U}} + \tilde{\mathbf{B}}^{\mathrm{T}}_{\hat{\mathbf{U}}\mathbf{Q}} \frac{\partial^2 \Pi_{\mathbf{U}}}{\partial \hat{\mathbf{U}}\, \partial \mathbf{U}} + \tilde{\mathbf{B}}^{\mathrm{T}}_{\hat{\mathbf{U}}\mathbf{Q}} \frac{\partial^2 \Pi_{\mathbf{U}}}{\partial \hat{\mathbf{U}}\, \partial \hat{\mathbf{U}}} \tilde{\mathbf{B}}_{\hat{\mathbf{U}}\mathbf{U}}, \tag{61}$$

$$\mathbf{K}_{\mathbf{UU}} = \frac{\partial^2 \Pi_{\mathbf{U}}}{\partial \mathbf{U}\, \partial \mathbf{U}} + \tilde{\mathbf{B}}^{\mathrm{T}}_{\hat{\mathbf{U}}\mathbf{U}} \frac{\partial^2 \Pi_{\mathbf{U}}}{\partial \hat{\mathbf{U}}\, \partial \mathbf{U}} + \frac{\partial^2 \Pi_{\mathbf{U}}}{\partial \mathbf{U}\, \partial \hat{\mathbf{U}}} \tilde{\mathbf{B}}_{\hat{\mathbf{U}}\mathbf{U}} + \tilde{\mathbf{B}}^{\mathrm{T}}_{\hat{\mathbf{U}}\mathbf{U}} \frac{\partial^2 \Pi_{\mathbf{U}}}{\partial \hat{\mathbf{U}}\, \partial \hat{\mathbf{U}}} \tilde{\mathbf{B}}_{\hat{\mathbf{U}}\mathbf{U}} + \tilde{\mathbf{B}}^{\mathrm{T}}_{\hat{\mathbf{Q}}\mathbf{U}} \frac{\partial^2 \Pi_{\mathbf{Q}}}{\partial \hat{\mathbf{Q}}\, \partial \hat{\mathbf{Q}}} \tilde{\mathbf{B}}_{\hat{\mathbf{Q}}\mathbf{U}}. \tag{62}$$

5. Correction to the Cauchy–Born rule in the overlap region

The previous sections describe how atomistic and continuum degrees of freedom are coupled; however, the specific form of the total potential has not yet been given. Naturally, the atomistic contribution to the potential energy is computed from a sum of bond energies in the crystal. The continuum strain energy is computed using the Cauchy–Born rule [10,11], which accurately describes the long wavelength behavior of the lattice. A critical detail to address is how one corrects for the overlap of the continuum and the underlying crystal. The proposed coupling method covers the entire domain with finite elements, but prescribes the motion of select portions of the mesh using an underlying atomistic crystal. Around the edges of the embedded crystals, there will be some region over which there is overlap between the bonds between free and ghost atoms and finite elements containing nodes with both free and prescribed displacements. In this overlap region, the weighting of the contributions to potential energy from the bonds and finite elements needs to be determined in such a way that the total energy for the coupled system is consistent with the result one would obtain from a pure atomistic system, regardless of the location and orientation of the embedded crystals with respect to the overlaying finite element mesh.

We can determine immediately that the weighting of the bonds between free and ghost atoms must always be 1 to preserve the energy per atom among free atoms, while the weighting of contributions from elements containing both active nodes and ghost atoms must be compensated to maintain the correct strain energy density. An initial attempt to quantify this weighting factor can be made by considering elements with uniform strain energy density, and by expressing the total strain energy in the continuum as

$$\Pi_{\mathrm{U}} = \sum_{e}^{N_e} w_e \Phi_e V_e, \tag{63}$$

where Φ_e and V_e are the strain energy density and volume, respectively, of element e and all elements $e \in N_e$ contribute energy according to a weighting factor w_e. For elements with no underlying atomic lattice, $w_e = 1$, while for elements that are bounded only by nodes with displacements projected from the underlying atomic lattice, $w_e = 0$. For overlap elements that contain ghost atoms and are bounded by both free and prescribed nodes, $0 \leqslant w_e \leqslant 1$. Note that the problem of finding these weights is underdetermined if one only considers the total energy of the system. That is, any number of combinations of weights can be found that reproduce the same total energy for the coupled system under homogeneous deformations. However, only one combination maintains the homogeneously deformed state as the lowest energy configuration. For simple one-dimensional examples, one can deduce the weights w_e. For the case of pair interactions, the weighing for these elements, assuming homogeneous stretching over the entire system, is

$$w_e = 1 - \frac{\sum_{\alpha\beta} \hat{r}_e^{(\alpha\beta)} \varphi^{(\alpha\beta)}}{V_e \Phi_e}, \tag{64}$$

where $\hat{r}_e^{(\alpha\beta)}$ is the fraction of the bond between atoms α and β that lies within the element and $\varphi^{(\alpha\beta)}$ is bond energy. Given that Φ_e is calculated for the continuum using the same bond potentials and orientations as for the crystal subject to the Cauchy–Born rule, it may be possible to express the weight w_e in a way that is independent of the state of deformation. That is, w_e must be expressed strictly in terms of the geometric parameters $\hat{r}_e^{(\alpha\beta)}$ and V_e, independent of Φ_e and $\varphi^{(\alpha\beta)}$; otherwise, the weighting factor would appear to be a function of the deformation even for the case of homogeneous deformation. If one uses elements with dimensions that are multiples of the crystal's unit cell, elements completely covering the underlying crystal have $w_e = 0$ since the strain energy density following the Cauchy–Born rule dictates

$$\Phi_e = \frac{1}{V_e} \sum_{\alpha\beta} \varphi^{(\alpha\beta)}. \tag{65}$$

For the extension to multiple dimensions and nonuniform strain energy density within elements, a general approach for introducing weighting into the total potential must be developed as well as a method for determining the optimal weighting, where optimality is associated with maintaining the homogeneously deformed state as the lowest energy configuration. The approach for introducing weighting into the total potential follows

directly from the Cauchy–Born rule. A generalized form of the Cauchy–Born rule for particles interacting with pair potentials was introduced by Gao and Klein in their virtual internal bond model (VIB) [26,27]. The VIB form of the strain energy density function is

$$\Phi = \frac{1}{V_0}\int_{V_0^*} U(r) D \, \mathrm{d}V, \tag{66}$$

where V_0 is the undeformed representative volume, r is the deformed virtual bond length, $U(r)$ is the bonding potential, D is the volumetric bond density function, and V_0^* is the integration volume defined by the range of influence of U. Depending on the range of influence of the bond potential function, the integration volume V_0^* may not correspond with the representative volume V_0. This difference may be illustrated for crystalline materials whenever the bond potentials extend beyond the lattice unit cell. The precise definition of $D(R,\theta,\phi)$ is that $D(R,\theta,\phi)R^2\sin\theta \, \mathrm{d}R \, \mathrm{d}\theta \, \mathrm{d}\phi$ represents the number of bonds in the undeformed solid with length between R and $R + \mathrm{d}R$ and orientation between $\{\theta,\phi\}$ and $\{\theta + \mathrm{d}\theta, \phi + \mathrm{d}\phi\}$. The case

$$D(R,\theta,\phi) = \delta_{\mathrm{D}}(R - R_0) D_{\theta\phi}(\theta,\phi) \tag{67}$$

corresponds to a network of identical bonds of undeformed length R_0. The Dirac delta function is denoted here with δ_{D}. A crystal lattice with a single-atom basis, e.g., a face-centered cubic lattice, for which interactions are limited to only nearest neighbors can be represented as

$$D(R,\theta,\phi) = D_0 \delta_{\mathrm{D}}(R - R_0) \sum_{m=1}^{M}\sum_{n=1}^{N} \frac{1}{\sin\theta}\delta_{\mathrm{D}}(\theta - \theta_m)\delta_{\mathrm{D}}(\phi - \phi_n), \tag{68}$$

where D_0 is a scaling constant and θ_m and ϕ_n are the orientation angles for the neighboring atoms. Each bond in $D(R,\theta,\phi)$ is representative of all bonds in the crystal with the same orientation and length.

For the coupled system, the bond density function needs to be modified as

$$D(R,\theta,\phi,\mathbf{X}) = D_0 \delta_{\mathrm{D}}(R - R_0) \sum_{m=1}^{M}\sum_{n=1}^{N} \frac{1}{\sin\theta}\delta_{\mathrm{D}}(\theta - \theta_m)\delta_{\mathrm{D}}(\phi - \phi_n)\rho_{mn}(\mathbf{X}), \tag{69}$$

where the spatially varying $0 \leqslant \rho_{mn}(\mathbf{X}) \leqslant 1$ is introduced because the energy contained by bonds between atoms that are explicitly represented, such as between free atoms and other free atoms or free atoms and ghost atoms, is already contributing to $\Pi_{\mathbf{Q}}$. Hence, that energy does not need to be accounted for in $\Pi_{\mathbf{U}}$. In regions of the domain superposed by a complete underlying crystal, $\rho_{mn}(\mathbf{X}) = 0$ since all bonds are represented at the density of the crystal. Conversely, $\rho_{mn}(\mathbf{X}) = 1$ over the parts of the domain without any underlying crystal since the Cauchy–Born strain energy density must account for all of the potential energy. In general, the strain energy for a crystal subject to pair interactions can be expressed as the sum

$$\Phi(\mathbf{C},\mathbf{X}) = \frac{1}{V_0}\sum_{i}^{n_b} \rho_{(i)}(\mathbf{X})\varphi(r_{(i)}), \tag{70}$$

where φ is the interaction potential,

$$r_{(i)} = \sqrt{\mathbf{R}_{(i)} \cdot \mathbf{C}\mathbf{R}_{(i)}}, \quad \mathbf{C} = \mathbf{F}^{\mathrm{T}}\mathbf{F}, \tag{71}$$

$\mathbf{R}_{(i)}$ is the vector representing bond (i) in the undeformed configuration and $\mathbf{F}$ is the deformation gradient. In this paper, (i) refers to not just a single bond, but rather all bonds of the same type, meaning bonds having the same orientation and length in the reference configuration. Hence, n_b is the total number of bond types.

In considering how this generalization of the Cauchy–Born rule is to be applied to our formulation, we recast the equilibrium equation (31) into

$$\mathbf{R}_{\mathbf{Q}} = \frac{\partial \Pi_{\mathbf{Q}}}{\partial \mathbf{Q}} + \mathbf{B}^{\mathrm{T}}_{\hat{\mathbf{U}}\mathbf{Q}}\mathbf{R}_{\hat{\mathbf{U}}} = 0 \tag{72}$$

for the L_2 projection or equilibrium equation (58) into

$$\mathbf{R}_{\mathbf{Q}} = \frac{\partial \Pi_{\mathbf{Q}}}{\partial \mathbf{Q}} + \tilde{\mathbf{N}}^{\mathrm{T}}_{\hat{\mathbf{U}}\mathbf{Q}}\mathbf{R}_{\hat{\mathbf{U}}} = 0 \tag{73}$$

for the MLS projection method where

$$\mathbf{R}_{\hat{\mathbf{U}}} = \frac{\partial \Pi_{\mathbf{U}}}{\partial \hat{\mathbf{U}}} + \mathbf{N}^{\mathrm{T}}_{\hat{\mathbf{Q}}\hat{\mathbf{U}}} \frac{\partial \Pi_{\mathbf{Q}}}{\partial \hat{\mathbf{Q}}}, \tag{74}$$

and we have omitted the external force term since, in general, such forces will not be acting on atoms in the overlap region. The quantity $\mathbf{R}_{\hat{\mathbf{U}}}$ represents the residual forces acting on prescribed nodes. Contributions to these forces come from both other nodes through derivatives of continuum strain energy and ghost atoms through derivatives of atomic potential energy. Similarly, Eqs. (32) and (59) can be recast as

$$\mathbf{R}_{\mathbf{U}} = \frac{\partial \Pi_{\mathbf{U}}}{\partial \mathbf{U}} + \mathbf{N}^{\mathrm{T}}_{\hat{\mathbf{Q}}\mathbf{U}} \frac{\partial \Pi_{\mathbf{Q}}}{\partial \hat{\mathbf{Q}}} + \mathbf{B}^{\mathrm{T}}_{\hat{\mathbf{U}}\mathbf{U}} \mathbf{R}_{\hat{\mathbf{U}}} = 0 \tag{75}$$

and

$$\mathbf{R}_{\mathbf{U}} = \frac{\partial \Pi_{\mathbf{U}}}{\partial \mathbf{U}} + \mathbf{N}^{\mathrm{T}}_{\hat{\mathbf{Q}}\mathbf{U}} \frac{\partial \Pi_{\mathbf{Q}}}{\partial \hat{\mathbf{Q}}} + \tilde{\mathbf{B}}^{\mathrm{T}}_{\hat{\mathbf{U}}\mathbf{U}} \mathbf{R}_{\hat{\mathbf{U}}} = 0, \tag{76}$$

respectively. We notice that the first two terms on the right-hand side of either (75) or (76) are very similar to the terms that define $\mathbf{R}_{\hat{\mathbf{U}}}$ and that an additional contribution exists for situations in which both free and prescribed nodes interact with free atoms through the quantities $\mathbf{B}_{\hat{\mathbf{U}}\mathbf{U}}$ and $\tilde{\mathbf{B}}_{\hat{\mathbf{U}}\mathbf{U}}$, respectively. While further analysis shown will use the equations corresponding to the MLS projection method, these relations prove that an equivalent analysis could be developed for the L_2 method.

We now decompose the contribution to the total energy from the continuum (28) as

$$\Pi_{\mathbf{U}} = \sum_{i}^{n_b} [\Pi_{\mathbf{U}}]_{(i)}, \tag{77}$$

where

$$[\Pi_{\mathbf{U}}]_{(i)} = [\Pi'_{\mathbf{U}}]_{(i)} + [\tilde{\Pi}_{\mathbf{U}}]_{(i)} + [\bar{\Pi}_{\mathbf{U}}]_{(i)}. \tag{78}$$

$[\Pi'_{\mathbf{U}}]_{(i)}$ represents the contribution over the domain where $\rho_{(i)} = 0$, which in the undeformed configuration will be denoted $\Omega'_{0(i)}$, $[\tilde{\Pi}_{\mathbf{U}}]_{(i)}$ represents the contribution over the domain where $0 < \rho_{(i)} < 1$, which in the undeformed configuration will be denoted $\tilde{\Omega}_{0(i)}$, and $[\bar{\Pi}_{\mathbf{U}}]_{(i)}$ represents the contribution over the domain where $\rho_{(i)} = 1$, which in the undeformed configuration will be denoted $\bar{\Omega}_{0(i)}$. Clearly, $[\Pi'_{\mathbf{U}}]_{(i)} = 0$. However, for completeness the decomposed domain in the undeformed configuration is defined as

$$\Omega_0 = \Omega'_{0(i)} \cup \tilde{\Omega}_{0(i)} \cup \bar{\Omega}_{0(i)}, \tag{79}$$

where

$$\Omega'_{0(i)} \cap \tilde{\Omega}_{0(i)} = \emptyset, \quad \tilde{\Omega}_{0(i)} \cap \bar{\Omega}_{0(i)} = \emptyset, \quad \bar{\Omega}_{0(i)} \cap \Omega'_{0(i)} = \emptyset. \tag{80}$$

Notice in (79) that while each of the decomposed domain sub-regions depends on the bond (i) being considered, the total domain Ω_0 refers to the entire volume of the system and no bond designation is necessary. The contribution to the strain energy from the bonds of type (i) represented in the continuum is given by

$$[\tilde{\Pi}_{\mathbf{U}}]_{(i)} = \frac{1}{V_0} \int_{\tilde{\Omega}_{0(i)}} \rho_{(i)}(\mathbf{X}) \varphi(r_{(i)}) \, \mathrm{d}\Omega, \tag{81}$$

$$[\bar{\Pi}_{\mathbf{U}}]_{(i)} = \frac{1}{V_0} \int_{\bar{\Omega}_{0(i)}} \varphi(r_{(i)}) \, \mathrm{d}\Omega. \tag{82}$$

In (81), the spatially varying bond density is introduced to account for the overlap between the continuum domain and the underlying crystal. We must still define how these bond densities are determined. For bonds $\mathbf{r}^{(\alpha\beta)}$ with atoms α and β both within given volume, such as a finite element, the contribution of $\mathbf{r}^{(\alpha\beta)}$ to the bond density of the volume is clear; however, if either α or β lies outside the volume, the fraction of the bond to attribute to this volume is not clear. Considering fractions of the bond length is an arbitrary construction that is only defined unambiguously in one-dimensional systems. However, in multiple dimensions bond fractions

may lie outside the elements containing either α or β, as illustrated in Fig. 2, even when the atomic spacing is much smaller than the element dimensions. In Fig. 2, the bond between atoms α and β is shown to overlap an element containing by node B. However, it is unclear whether this bond should exert forces on node B since neither atom α nor atom β lies within any elements within the support of nodes B. For multi-body interactions, the division of the bond energy in space is even more difficult to define unambiguously.

To avoid the ambiguity associated with partitioning a bond, we determine the bond densities in (81) based on a consistency condition. The coupled system should produce homogeneous deformations given the appropriate boundary conditions. This concept is analogous to the "patch test" for assessing the convergence of the FE method [22]. One could consider the unstressed system, but in general we would like to satisfy this consistency condition for any homogeneous state of deformation which the atomistic or continuum system would produce individually. For the atoms $\alpha \in \mathscr{A}$ which are not located near surfaces or other crystal defects, this condition is satisfied automatically. These atoms only interact with other atoms in $\mathscr{A}$ or with the ghost atoms in $\hat{\mathscr{A}}$ which have been introduced to provide a complete surrounding. Hence, in evaluating Eq. (73), the term $\frac{\partial \Pi_{\mathbf{Q}}}{\partial \mathbf{Q}}$ is set to zero and we are left with the relation $\mathbf{R}_{\hat{\mathbf{U}}} = 0$. This makes sense; the free atoms are equilibrated through their interaction with other free atoms and ghost atoms, while the continuum densities $\rho_{(i)}(\mathbf{X})$ need to be determined such that the prescribed nodes are also in equilibrium.

For nodes whose support lies entirely in $\bar{\Omega}_{0(i)}$, the homogeneous solution will be reproduced as long as the element formulation satisfies the patch test. However, for nodes $a \in \check{\mathscr{N}}$ whose support intersects $\tilde{\Omega}_{0(i)}$, this consistency condition is not guaranteed. Let $\Omega_0^{(a)}$ denote the support of node a in the undeformed configuration, as illustrated in Fig. 3. We define $\tilde{\mathscr{N}}_{(i)}$ as the subset of $\check{\mathscr{N}}$ containing all nodes satisfying

$$\Omega_0^{(a)} \cap \tilde{\Omega}_{0(i)} \equiv \tilde{\Omega}_{0(i)}^{(a)} \neq \emptyset. \tag{83}$$

We begin the derivation of this consistency condition by considering a general state of homogeneous deformation, which may be expressed as

$$\mathbf{u}(\mathbf{X}, t) = \mathbf{c}(t) + \mathbf{Q}(t)\mathbf{F}^{*}\mathbf{X}, \tag{84}$$

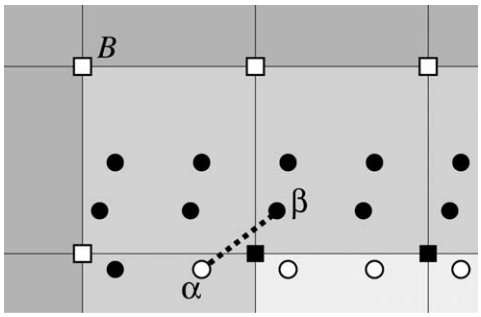

Fig. 2. Bond between atoms near element boundaries.

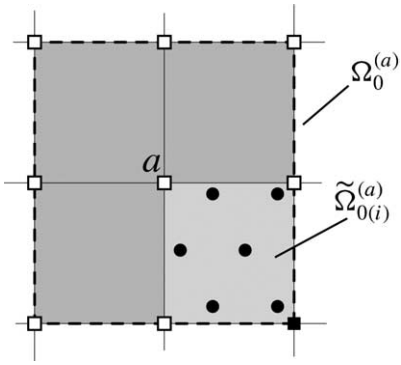

Fig. 3. The support of node $a \in \tilde{\mathscr{N}}_{(i)}$.

where $\mathbf{c}(t)$ is a rigid body translation, $\mathbf{Q}(t)$ is a rigid body rotation, and $\mathbf{F}^*$ is the homogeneous deformation gradient over the entire domain. Since all contributions to the total potential are frame invariant, we can consider the following state of homogeneous deformation

$$\mathbf{x} = \mathbf{F}^*\mathbf{X} \quad \text{and} \quad \mathbf{u} = (\mathbf{F}^* - \mathbf{1})\mathbf{X} \tag{85}$$

without loss of generality. In determining the total internal force on a node in $\tilde{\mathcal{N}}_{(i)}$, we find three types of contributions. There are continuum contributions from $[\tilde{\Pi}_{\mathbf{U}}]_{(i)}$ and $[\bar{\Pi}_{\mathbf{U}}]_{(i)}$, and a third contribution from bonds between free atoms in either $\Omega'_{0(i)}$ or $\tilde{\Omega}^{(a)}_{0(i)}$ and ghost atoms in $\tilde{\Omega}^{(a)}_{0(i)}$, represented by the terms $\mathbf{N}^{\mathrm{T}}_{\hat{\mathbf{Q}}\hat{\mathbf{U}}}\frac{\partial \Pi_{\mathbf{Q}}}{\partial \hat{\mathbf{Q}}}$ in (74) or $\mathbf{N}^{\mathrm{T}}_{\hat{\mathbf{Q}}\mathbf{U}}\frac{\partial \Pi_{\mathbf{Q}}}{\partial \hat{\mathbf{Q}}}$ in (76).

First, we consider the atomistic contribution. The potential energy in the bonds is given by

$$\Pi_{\mathbf{Q}} = \sum_{\alpha}\sum_{\beta\neq\alpha}\varphi(r^{(\alpha\beta)}). \tag{86}$$

The atomistic contribution to the force on a node in $\tilde{\mathcal{N}}_{(i)}$ is given by

$$\mathbf{f}^{(a)}_{\mathbf{Q}} = -\frac{\partial \Pi_{\mathbf{Q}}}{\partial \mathbf{u}^{(a)}}, \quad a \in \tilde{\mathcal{N}}_{(i)}. \tag{87}$$

For this analysis, we examine the total force on node (a) which includes contributions from all bond types $i = 1,2,\ldots,n_b$ as long as there is at least a single bond type for which $a \in \tilde{\mathcal{N}}_{(i)}$. We shall show later that for those bonds for which $a \notin \tilde{\mathcal{N}}_{(i)}$, the expression for total force evaluates to zero. The only bonds contributing to $\mathbf{f}^{(a)}_{\mathbf{Q}}$ are those between free atom (α), which resides in either $\Omega'_{0(i)}$ or $\tilde{\Omega}^{(a)}_{0(i)}$, and ghost atom (β), which resides in $\tilde{\Omega}^{(a)}_{0(i)}$. The bond vector may be expressed as

$$\begin{aligned}\mathbf{r}^{(\alpha\beta)} &= \mathbf{x}^{(\beta)} - \mathbf{x}^{(\alpha)} = [\mathbf{X}^{(\beta)} + \mathbf{u}(\mathbf{X}^{(\beta)})] - [\mathbf{X}^{(\alpha)} + \mathbf{q}^{(\alpha)}] = \mathbf{X}^{(\beta)} + \sum_{a\in\tilde{\mathcal{N}}_{(i)}} N^{(a)}(\mathbf{X}^{(\beta)})\mathbf{u}^{(a)} - \mathbf{X}^{(\alpha)} - \mathbf{q}^{(\alpha)} \\ &= \sum_{a\in\tilde{\mathcal{N}}_{(i)}} N^{(a)}(\mathbf{X}^{(\beta)})\mathbf{u}^{(a)} - \mathbf{q}^{(\alpha)} + \mathbf{R}^{(\alpha\beta)},\end{aligned} \tag{88}$$

and

$$\frac{\partial \mathbf{r}^{(\alpha\beta)}}{\partial \mathbf{u}^{(a)}} = N^{(a)}(\mathbf{X}^{(\beta)})\mathbf{1}, \tag{89}$$

where $N^{(a)}(\mathbf{X})$ is an element of either $\mathbf{N}_{\hat{\mathbf{Q}}\mathbf{U}}$ or $\mathbf{N}_{\hat{\mathbf{Q}}\hat{\mathbf{U}}}$ depending on whether $a \in \mathcal{N}$ or $a \in \hat{\mathcal{N}}$, respectively. Using this result, $\mathbf{f}^{(a)}_{\mathbf{Q}}$ (87) may be expanded as

$$\mathbf{f}^{(a)}_{\mathbf{Q}} = -\mathbf{F}^*\sum_{\alpha\in\mathscr{A}}\sum_{\beta:\mathbf{X}^{(\beta)}\in\tilde{\Omega}^{(a)}_0}\frac{\varphi'(r^{(\alpha\beta)})}{r^{(\alpha\beta)}}\mathbf{R}^{(\alpha\beta)}N^{(a)}(\mathbf{X}^{(\beta)}). \tag{90}$$

The continuum contribution over $\bar{\Omega}_{0(i)}$ follows from

$$\bar{\mathbf{f}}^{(a)}_{\mathbf{U}} = -\sum_{i}^{n_b}\frac{\partial \bar{\Pi}_{\mathbf{U}(i)}}{\partial \mathbf{u}^{(a)}} = -\sum_{i}^{n_b}\frac{\partial}{\partial \mathbf{u}^{(a)}}\int_{\bar{\Omega}^{(a)}_{0(i)}}\Phi\,\mathrm{d}\Omega = -\sum_{i}^{n_b}\int_{\bar{\Omega}^{(a)}_{0(i)}}\mathbf{P}:\frac{\partial \mathbf{F}}{\partial \mathbf{u}^{(a)}}\,\mathrm{d}\Omega, \tag{91}$$

where $\bar{\Omega}^{(a)}_{0(i)} \equiv \bar{\Omega}_{0(i)} \cap \Omega^{(a)}_0$ and $\mathbf{P} = \frac{\partial \Phi}{\partial \mathbf{F}}$ is the non-symmetric, first Piola–Kirchhoff stress. From Φ given by (70), the Piola–Kirchhoff stress is

$$\mathbf{P} = \mathbf{F}\frac{1}{V_0}\sum_{i}^{n_b}\frac{\varphi'(r_{(i)})}{r_{(i)}}\mathbf{R}_{(i)}\otimes\mathbf{R}_{(i)}, \tag{92}$$

using the relations

$$\mathbf{r}_{(i)} = \mathbf{F}^*\mathbf{R}_{(i)} \quad \text{and} \quad \frac{\partial r_{(i)}}{\partial \mathbf{F}} = \frac{1}{r_{(i)}}\mathbf{r}_{(i)}\otimes\mathbf{R}_{(i)}. \tag{93}$$

Using

$$\frac{\partial F_{iJ}}{\partial u_k^{(a)}} = \frac{\partial N^{(a)}}{\partial X_J}\delta_{ik}, \tag{94}$$

we can expand $\bar{\mathbf{f}}_{\mathbf{U}}^{(a)}$ as

$$\bar{\mathbf{f}}_{\mathbf{U}}^{(a)} = -\mathbf{F}^* \frac{1}{V_0} \sum_i^{n_b} \int_{\bar{\Omega}_{0(i)}^{(a)}} \left[\frac{\varphi'(r)}{r}\mathbf{R}\otimes\mathbf{R}\right]_{(i)} \frac{\partial N^{(a)}}{\partial \mathbf{X}}\, \mathrm{d}\Omega. \tag{95}$$

The contribution from $[\tilde{I}I_{\mathbf{U}}]_{(i)}$ differs from (95) only by the introduction of the bond density function $\rho_{(i)}(\mathbf{X})$ for $i = 1,\ldots,n_b$ and the integration domain, and is given by

$$\tilde{\mathbf{f}}_{\mathbf{U}}^{(a)} = -\sum_i^{n_b} \frac{\partial \tilde{I}I_{\mathbf{U}(i)}}{\partial \mathbf{u}^{(a)}} = -\mathbf{F}^* \frac{1}{V_0} \sum_i^{n_b} \int_{\tilde{\Omega}_{0(i)}^{(a)}} \left[\frac{\varphi'(r)\rho}{r}\mathbf{R}\otimes\mathbf{R}\right]_{(i)} \frac{\partial N^{(a)}}{\partial \mathbf{X}}\, \mathrm{d}\Omega. \tag{96}$$

Many terms in the integrands of (95) and (96) do not vary spatially if the body is in a state of homogeneous deformation. Therefore, we can rewrite these expressions as

$$\bar{\mathbf{f}}_{\mathbf{U}}^{(a)} = -\mathbf{F}^* \frac{1}{V_0} \sum_i^{n_b} \left[\frac{\varphi'(r)}{r}\mathbf{R}\otimes\mathbf{R}\right]_{(i)} \int_{\bar{\Omega}_{0(i)}^{(a)}} \frac{\partial N^{(a)}}{\partial \mathbf{X}}\, \mathrm{d}\Omega \tag{97}$$

and

$$\tilde{\mathbf{f}}_{\mathbf{U}}^{(a)} = -\mathbf{F}^* \frac{1}{V_0} \sum_i^{n_b} \left[\frac{\varphi'(r)}{r}\mathbf{R}\otimes\mathbf{R}\right]_{(i)} \int_{\tilde{\Omega}_{0(i)}^{(a)}} \rho_{(i)} \frac{\partial N^{(a)}}{\partial \mathbf{X}}\, \mathrm{d}\Omega. \tag{98}$$

Since the Cauchy–Born expressions for the continuum response are selected to represent the crystal structure of the underlying atomistic system, the bonds in (90) may be collected into the same groups by orientation and length as those given by the bond types $i = 1,\ldots,n_b$ in (97) and (98). Using this observation, $\mathbf{f}_{\mathbf{Q}}^{(a)}$ from (90) may be expressed as

$$\mathbf{f}_{\mathbf{Q}}^{(a)} = -\mathbf{F}^* \sum_i^{n_b} \left[\frac{\varphi'(r)}{r}\mathbf{R} \sum_{\substack{\beta:\mathbf{X}^{(\beta)}\in\bar{\Omega}_0^{(a)},\\ \mathbf{R}^{(\alpha\beta)}=\mathbf{R}}} N^{(a)}(\mathbf{X}^{(\beta)})\right]_{(i)}. \tag{99}$$

Collecting these expressions for the force on a node in $\tilde{\mathcal{N}}_{(i)}$, we find

$$\mathbf{f}^{(a)} = \mathbf{f}_{\mathbf{Q}}^{(a)} + \bar{\mathbf{f}}_{\mathbf{U}}^{(a)} + \tilde{\mathbf{f}}_{\mathbf{U}}^{(a)} = -\mathbf{F}^* \sum_i^{n_b} \left[\frac{\varphi'(r)}{r}\right]_{(i)} \hat{\mathbf{f}}_{(i)}^{(a)}, \tag{100}$$

where

$$\hat{\mathbf{f}}_{(i)}^{(a)} = \mathbf{R}_{(i)} \sum_{\substack{\beta:\mathbf{X}^{(\beta)}\in\bar{\Omega}_{0(i)}^{(a)},\\ \mathbf{R}^{(\alpha\beta)}=\mathbf{R}_{(i)}}} N^{(a)}(\mathbf{X}^{(\beta)}) + \frac{1}{V_0}[\mathbf{R}\otimes\mathbf{R}]_{(i)} \left[\int_{\bar{\Omega}_{0(i)}^{(a)}} \frac{\partial N^{(a)}}{\partial \mathbf{X}}\, \mathrm{d}\Omega + \int_{\tilde{\Omega}_{0(i)}^{(a)}} \rho_{(i)} \frac{\partial N^{(a)}}{\partial \mathbf{X}}\, \mathrm{d}\Omega\right]. \tag{101}$$

Note that $\hat{\mathbf{f}}_{(i)}^{(a)}$ in (101) has units of length, and thus can be directly interpreted as bond overlap. Also, it is independent of the homogeneous state of deformation, depending only on the geometry of the undeformed configuration.

Earlier, we mentioned that (101) is evaluated for any node (a) such that $a \in \tilde{\mathcal{N}}_{(i)}$ for at least one bond type (i). For any bond type (i) for which $a \notin \tilde{\mathcal{N}}_{(i)}$, it can be shown that (101) evaluates to zero. For such atoms, $\tilde{\Omega}_{0(i)}^{(a)} = \emptyset$ and $\bar{\Omega}_{0(i)}^{(a)} = \Omega_0^{(a)}$. Thus, (101) simplifies to

$$\hat{\mathbf{f}}_{(i)}^{(a)} = \frac{1}{V_0}[\mathbf{R}\otimes\mathbf{R}]_{(i)} \int_{\Omega_0^{(a)}} \frac{\partial N^{(a)}}{\partial \mathbf{X}}\, \mathrm{d}\Omega. \tag{102}$$

The integral of the gradient of a nodal shape function over its support is

$$\int_{\Omega_0^{(a)}} \frac{\partial N^{(a)}}{\partial \mathbf{X}}\, \mathrm{d}\Omega = \oint_{\partial\Omega_0^{(a)}} N^{(a)}\mathbf{N}\, \mathrm{d}\Gamma = 0, \tag{103}$$

where $\mathbf{N}$ is the outward normal over $\partial\Omega_0^{(a)}$, the boundary of the support of node (a). We can combine (102) and (103) to produce $\hat{\mathbf{f}}_{(i)}^{(a)} = 0$.

The expressions for nodal force presented in Eqs. (100) and (101) result in the equilibration of prescribed nodes by satisfying the relation $\mathbf{R}_{\hat{\mathbf{U}}} = 0$. If the bond density functions are determined such that this equality is exact, then the same expressions can be used to satisfy equilibration of free nodes through the relation $\mathbf{R}_{\mathbf{U}} = 0$ as it appears in Eq. (76). However, if equilibration of prescribed nodes is only approximately satisfied, Eq. (76) contains an additional term that must be evaluated for free nodes. For this situation,

$$\mathbf{f}^{(a)} = -\mathbf{F}^* \sum_i^{n_b} \left[\frac{\varphi'(r)}{r}\right]_{(i)} \mathbf{f}_{(i)}^{(a)}, \quad a \in \mathscr{N}, \tag{104}$$

where

$$\mathbf{f}_{(i)}^{(a)} = \hat{\mathbf{f}}_{(i)}^{(a)} + \sum_{b \in \tilde{\mathscr{N}}_i \cap \hat{\mathscr{N}}} \hat{\mathbf{f}}_{(i)}^{(b)} \tilde{B}^{(a)}(\mathbf{X}^{(\mathbf{b})}), \tag{105}$$

and where the term $\tilde{B}^{(a)}(\mathbf{X}^{(b)})$ refers to the element of $\tilde{\mathbf{B}}_{\hat{\mathbf{U}}\mathbf{U}}$ corresponding with nodes $a \in \mathscr{N}$ and $b \in \hat{\mathscr{N}}$.

If we define the quantity $\tilde{\mathbf{R}}$ to be

$$\tilde{\mathbf{R}} = [\mathbf{f}^{(a)}]^{\mathrm{T}}, \quad a \in \tilde{\mathscr{N}}_{(i)}, \tag{106}$$

then in the absence of external loads being imposed directly on the nodes in $\tilde{\mathscr{N}}_{(i)}$, we would expect $\|\tilde{\mathbf{R}}\| = 0$ for all states of deformation. For the case of homogeneous deformation, this amounts to enforcing the conditions of $\hat{\mathbf{f}}_{(i)}^{(a)} = 0$ or $\mathbf{f}_{(i)}^{(a)} = 0$, where a is either a prescribed node or a free node, respectively, for all $i = 1, \ldots, n_b$ and $a \in \tilde{\mathscr{N}}_{(i)}$. This implies (101) and (105) provide a means for defining the discretized values of $\rho_{(i)}$ optimally. In most situations, the discretization of the bond density $\rho_{(i)}$ may be insufficient to capture the local fluctuation in the bond density required to produce both $\hat{\mathbf{f}}_{(i)}^{(a)} = 0$ and $\mathbf{f}_{(i)}^{(a)} = 0$ exactly (thereby necessitating the distinction between $\hat{\mathbf{f}}_{(i)}^{(a)}$ and $\mathbf{f}_{(i)}^{(a)}$ as discussed earlier). Therefore, we approximate these conditions by introducing

$$P_{(i)} = \frac{1}{2}\left(\sum_{a \in \tilde{\mathscr{N}}_i \cap \mathscr{N}} \mathbf{f}_{(i)}^{(a)} \cdot \mathbf{f}_{(i)}^{(a)} + \sum_{a \in \tilde{\mathscr{N}}_i \cap \hat{\mathscr{N}}} \hat{\mathbf{f}}_{(i)}^{(a)} \cdot \hat{\mathbf{f}}_{(i)}^{(a)}\right) \tag{107}$$

and then select $\boldsymbol{\rho}_{(i)}$ that satisfies

$$\min_{\boldsymbol{\rho}_{(i)}} [P_{(i)}], \tag{108}$$

where $\boldsymbol{\rho}_{(i)}$ represents the vector of values for all FE integration points at which we are evaluating $\rho_{(i)}(\mathbf{X})$. The expression for $\hat{\mathbf{f}}_{(i)}^{(a)}$ given in (101) suggests an alternative form for the quantity $P_{(i)}$ requiring a simpler calculation of $\mathbf{R}_{(i)} \cdot \hat{\mathbf{f}}_{(i)}^{(a)}$ in place of $\hat{\mathbf{f}}_{(i)}^{(a)} \cdot \hat{\mathbf{f}}_{(i)}^{(a)}$ since $\hat{\mathbf{f}}_{(i)}^{(a)}$ is collinear with $\mathbf{R}_{(i)}$. The same argument can be made for the term in $P_{(i)}$ involving $\mathbf{f}_{(i)}^{(a)}$ producing

$$P_{(i)} = \frac{1}{2}\left(\sum_{a \in \tilde{\mathscr{N}}_i \cap \mathscr{N}} \left[\mathbf{R}_{(i)} \cdot \mathbf{f}_{(i)}^{(a)}\right]^2 + \sum_{a \in \tilde{\mathscr{N}}_i \cap \hat{\mathscr{N}}} \left[\mathbf{R}_{(i)} \cdot \hat{\mathbf{f}}_{(i)}^{(a)}\right]^2\right). \tag{109}$$

The number of independent equations we can extract from $P_{(i)}$ is determined by the number of spatial dimensions and the number of nodes in $\tilde{\mathscr{N}}_{(i)}$. We cannot uniquely determine $\boldsymbol{\rho}_{(i)}$ if it possesses more unknowns. If we introduce unknowns at the integration points used for the finite element calculations, the number of unknowns is determined by the number of elements covering $\tilde{\Omega}_{0(i)}$ and the number of integration points per element. Clearly, the number of unknowns may generally exceed the number of independent equations. Therefore, it

may be necessary to introduce an additional term into either (107) or (109) to ensure the solution of $\boldsymbol{\rho}_{(i)}$. One possible addition is a term that tends to smooth the bond density distribution, resulting in the modified function

$$P^*_{(i)} = P_{(i)} + \frac{1}{2}\kappa \int_{\tilde{\Omega}_{0(i)}} \nabla_{\mathbf{X}}\rho_{(i)} \cdot \nabla_{\mathbf{X}}\rho_{(i)}\, \mathrm{d}\Omega, \tag{110}$$

and $\rho_{(i)}$ satisfies

$$\min_{\boldsymbol{\rho}_{(i)}}[P^*_{(i)}], \tag{111}$$

where κ is a parameter used to adjust the influence of the gradient regularization. This method is known as Tikhonov regularization and is commonly found in the literature [28]. The stability of determining $\boldsymbol{\rho}_{(i)}$ for general cases of overlap between the crystal and mesh needs to be investigated further.

In summary, the continuum strain energy for overlap elements is calculated using a modification of the Cauchy–Born rule that includes bond density correction functions, $\rho_{(i)}(\mathbf{X})$. These functions are determined by solving the minimization problems given in Eqs. (109)–(111) using the expressions for $\hat{\mathbf{f}}^{(a)}_{(i)}$ given in Eq. (101) and $\mathbf{f}^{(a)}_{(i)}$ given in Eq. (105). For our analyses, we use a Newton solution scheme to solve for the vector of values $\boldsymbol{\rho}_{(i)}$ subject to the constraint $0 \leqslant \rho_{(i)} \leqslant 1$.

6. Implications of the overlap correction

Examination of (101) allows us to determine the fictitious forces acting on nodes in $\tilde{\mathcal{N}}_{(i)}$ if no correction is made to the Cauchy–Born rule. In this case, the uncorrected bond density function is $\rho_{(i)}(\mathbf{X}) = 1$ for all $i = 1,\ldots,n_b$, representing full density for all bond families n_b. Using (103) with the uncorrected bond density function, we find

$$\hat{\mathbf{f}}^{(a)}_{(i)} = \mathbf{R}_{(i)} \sum_{\substack{\beta:\mathbf{X}^{(\beta)}\in\tilde{\Omega}^{(a)}_{0(i)},\\ \mathbf{R}^{(\alpha\beta)}=\mathbf{R}_{(i)}}} N^{(a)}(\mathbf{X}^{(\beta)}). \tag{112}$$

Using Eqs. (100), (104), (105) and (112), we can determine the total fictitious force acting on nodes that bound the overlap region as a result of uncorrected overlap between the continuum and the underlying crystal.

Interpreting the expression for $\hat{\mathbf{f}}^{(a)}_{(i)}$ in (101) is difficult in general given that integration of the shape function gradient occurs over two distinct domains, $\bar{\Omega}^{(a)}_{0(i)}$ and $\tilde{\Omega}^{(a)}_{0(i)}$. However, detailed examination enables us to conclude that the total force on node (a) from bond type (i) comes from a combination of forces exerted on ghost atoms within the overlap element from free atoms and the force on the node exerted by the continuum to compensate for the bonds that are not present. At equilibrium, $\hat{\mathbf{f}}^{(a)}_{(i)} = 0$ for prescribed nodes, or $\mathbf{f}^{(a)}_{(i)} = 0$ for free nodes. It is interesting to note that this result can also be obtained by omitting the cross terms between nodes and ghost atoms in the equilibrium equations and by using the uncorrected Cauchy–Born rule within the overlap elements. The cross terms are those involving $\mathbf{N}_{\hat{\mathbf{Q}}\hat{\mathbf{U}}}$ in (74) and $\mathbf{N}_{\hat{\mathbf{Q}}\mathbf{U}}$ in (76). Without these terms, we find in (101) that

$$\mathbf{R}_{(i)} \sum_{\substack{\beta:\mathbf{X}^{(\beta)}\in\tilde{\Omega}^{(a)}_{0(i)},\\ \mathbf{R}^{(\alpha\beta)}=\mathbf{R}_{(i)}}} N^{(a)}(\mathbf{X}^{(\beta)}) \to 0, \tag{113}$$

while the uncorrected Cauchy–Born rule ($\rho_{(i)} = 1$) implies

$$\frac{1}{V_0}[\mathbf{R}\otimes\mathbf{R}]_{(i)}\left[\int_{\bar{\Omega}^{(a)}_{0(i)}} \frac{\partial N^{(a)}}{\partial \mathbf{X}}\, \mathrm{d}\Omega + \int_{\tilde{\Omega}^{(a)}_{0(i)}} \rho_{(i)} \frac{\partial N^{(a)}}{\partial \mathbf{X}}\, \mathrm{d}\Omega\right] \to \frac{1}{V_0}[\mathbf{R}\otimes\mathbf{R}]_{(i)} \int_{\Omega^{(a)}_0} \frac{\partial N^{(a)}}{\partial \mathbf{X}}\, \mathrm{d}\Omega = 0, \tag{114}$$

meaning the internal forces on free and prescribed nodes coming from element-level forces, $\frac{\partial \Pi_{\mathbf{U}}}{\partial \mathbf{U}}$ and $\frac{\partial \Pi_{\mathbf{U}}}{\partial \hat{\mathbf{U}}}$, respectively, are balanced. In effect, decoupling the atomistic and continuum analyses is accomplished by eliminating the influence of ghost atoms on nodes that border overlap elements combined with treating the overlap

element with the constitutive model derived from the normal Cauchy–Born rule as though the overlap element has no underlying crystal lattice present. Thus, the correct solution for the displacement field is obtained without regard to force cross terms. It is important to realize that *both* of the actions discussed above must be done for this to be true. If ghost atom influence is eliminated and a corrected Cauchy–Born rule is used, or vice versa, the solution obtained will be incorrect. It is also important to note that this ad hoc decoupling possesses the distinct disadvantage that an expression for the system potential energy no longer exists.

7. Example calculations

For all the numerical examples in this section, we use the meshless method described in Section 4 to project the fine scale solution from the atoms onto nodes in the overlaying finite element mesh. Solutions are calculated with a preconditioned conjugate gradient algorithm [23], using diagonal approximations to $\mathbf{K}_{\mathbf{QQ}}$ (60) and $\mathbf{K}_{\mathbf{UU}}$ (62). All calculations are solved to a relative tolerance on the residual of

$$\frac{\|[\mathbf{R}_{\mathbf{Q}}, \mathbf{R}_{\mathbf{U}}]^{\mathrm{T}}\|^{(i)}}{\|[\mathbf{R}_{\mathbf{Q}}, \mathbf{R}_{\mathbf{U}}]^{\mathrm{T}}\|^{(0)}} < 10^{-12} \tag{115}$$

for the ith iterate of the solution. The calculations are performed using a research-oriented program capable of both finite element analysis and atomistic simulation that was developed at Sandia National Laboratories [29].

7.1. One-dimensional examples

To demonstrate the key features of the coupling approach, consider the patch of a one-dimensional coupled system shown in Fig. 4. The patch consists of the complete support of node (a), which is comprised of two elements of dimension h, and a single pair bond of length R. For this system, bonds exist only between nearest neighbor atoms. Hence, the subscript (i) may be omitted since only a single type of atomic bonds exists for all atoms. The nodal shape function and derivative for this case is given by

$$N^{(a)}(X) = \begin{cases} 1 - \frac{X^{(a)} - X}{h}, & X \in \tilde{\Omega}_0^{(a)}, \\ 1 + \frac{X^{(a)} - X}{h}, & X \in \bar{\Omega}_0^{(a)}, \\ 0, & \text{elsewhere}, \end{cases} \quad \text{and} \quad \frac{\partial N^{(a)}(X)}{\partial X} = \begin{cases} \frac{1}{h}, & X \in \tilde{\Omega}_0^{(a)}, \\ -\frac{1}{h}, & X \in \bar{\Omega}_0^{(a)}, \\ 0, & \text{elsewhere}, \end{cases} \tag{116}$$

respectively. Using (101) and setting $\mathrm{f}^{(a)} = 0$, we find the optimal bond density must satisfy

$$\int_{\tilde{\Omega}_0^{(a)}} \rho \, \mathrm{d}X = h(1 - N^{(a)}(X^{(\beta)})) \quad \text{for } X^{(a)} - h \leqslant X^{(\beta)} \leqslant X^{(a)} - h + R, \tag{117}$$

which holds for

$$\rho = 1 - N^{(a)}(X^{(\beta)}) \tag{118}$$

over $\tilde{\Omega}_0^{(a)}$. Note that in this case, the problem of determining ρ does not have a unique solution if ρ is discretized with more than one unknown and more than one integration point is used to evaluate the left-hand side of

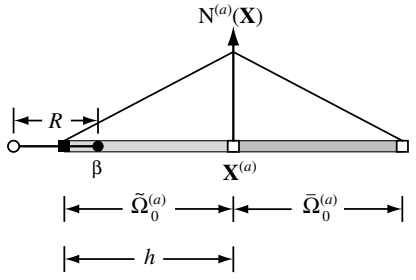

Fig. 4. Patch from a one-dimensional coupled system.

(117). For this example, we can see how the bond density simply compensates for the overlap in the continuum and the underlying lattice. As mentioned above, attributing fractions of a bond's energy to certain domains becomes ambiguous in multiple dimensions for which the general method for determining the bond density distribution becomes necessary. This point was not addressed by the authors of [8], who examined only one-dimensional chains of atoms with nearest neighbor interactions.

Fig. 5 shows the displacements of a coupled system composed of five nodes and five atoms. The sets of nodes with free and prescribed displacements are $\mathcal{N} = \{4, 5\}$ and $\hat{\mathcal{N}} = \{1, 2, 3\}$, respectively. The sets of atoms with free and prescribed displacements are $\mathscr{A} = \{1, 2, 3, 4\}$ and $\hat{\mathscr{A}} = \{5\}$, respectively. The chain of atoms is bound by the quadratic potential $\varphi(r) = \frac{1}{2}k(r - R)^2$ acting between nearest neighbors with $R = \frac{1}{2}$. From the Cauchy–Born rule, the elements, with dimension $h = 1$, have an initial modulus $E = Rk$. To demonstrate the effect of the bond density function, we prescribe $\rho(X) = 1$, meaning no correction is made for the overlap of elements and bonds between node 4 and atom 5. The system is loaded with the prescribed displacements $Q^{(1)} = X^{(1)} = \frac{1}{4}$ and $U^{(5)} = X^{(5)} = 4$, so that the homogeneously deformed shape should have a constant slope of 1. The results plotted in Fig. 5 show the coupled system does not deform homogeneously. The reduced slope in the element 3–4 is the result of increased stiffness of this region over the other parts of the system resulting from the overlap between bonds and elements. The slopes of the atomic chain 1–2–3–4 and element 4–5 are the same indicating the stiffness produced by the Cauchy–Born model is consistent with the lattice. Finally, we note that nodes 1, 2, and 3 lie on a straight line defined by displacements of the atomic chain 1–2–3–4, indicating that the method used to transfer the atomistic displacement to the nodes in $\hat{\mathcal{N}}$, an L_2 projection in this case is able to reproduce homogeneous displacements exactly. In order to reproduce the homogeneous solution, we must define $\rho(X) = \frac{3}{4}$ for $2 \leqslant X \leqslant 3$, as given by (118).

The simple example shown above of the homogeneously stretched one-dimensional atomic chain was performed using an L_2 projection method. Because of the computational cost, we seek alternatives to calculating $\mathbf{M}^{-1}_{\hat{\mathcal{U}}\hat{\mathcal{U}}}$ associated with the L_2 projection of atomistic displacements to the nodes in $\hat{\mathcal{N}}$. One simple alternative is to use a diagonal approximation to $\mathbf{M}_{\hat{\mathcal{U}}\hat{\mathcal{U}}}$, which has the structure of a finite element mass matrix. A number of "lumping" methods has been developed for the solution of dynamic problems with explicit time integration schemes. Fig. 6 shows the displacements for a coupled system with $\mathbf{M}_{\hat{\mathcal{U}}\hat{\mathcal{U}}}$ diagonalized using Hinton's method [30]. The results show that although all of the nodes in $\mathcal{N}$ and atoms in $\mathscr{A}$ follow the homogeneous solution $Q(X) = U(X) = X$, the nodes and atoms with prescribed motion, those in $\hat{\mathcal{N}}$ and $\hat{\mathscr{A}}$, respectively, do not follow the homogeneous solution. This solution is produced by defining the bond density $\rho(X) = \frac{6}{11}$ for $2 \leqslant X \leqslant 3$ and by weighting the energy of bond 4–5 as $\frac{16}{7}$, which are determined by requiring $\frac{\partial \Pi}{\partial Q^{(4)}} = 0$ and $\frac{\partial \Pi}{\partial U^{(4)}} = 0$ for the system with all active displacements following a homogeneously deformed solution. The additional weight of the 4–5 bond is required because the approximate L_2 projection, using the diagonalized form of $\mathbf{M}_{\hat{\mathcal{U}}\hat{\mathcal{U}}}$, is unable to reproduce homogeneous solutions exactly. The displacement field across nodes 1, 2, and 3 does vary homogeneously, but not with the correct slope. Consequently, atom 5 fails to lie on the solution with homogeneous deformation since it is constrained to lie on the solution between nodes 3 and 4. Further testing with this small

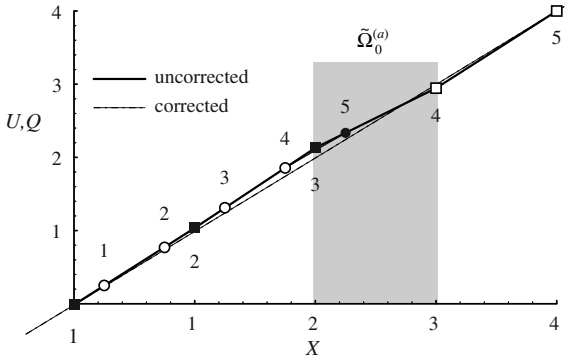

Fig. 5. Homogeneous displacements of the one-dimensional coupled system for both the corrected bond density of $\rho(X) = \frac{3}{4}$ and the uncorrected bond density of $\rho(X) = 1$. Free nodes, projected nodes, free atoms and ghost atoms are shown, respectively, as □, ■, ○ and ●. Atom and element numbers are given within the figure by the digit shown above or below, respectively, the corresponding part.

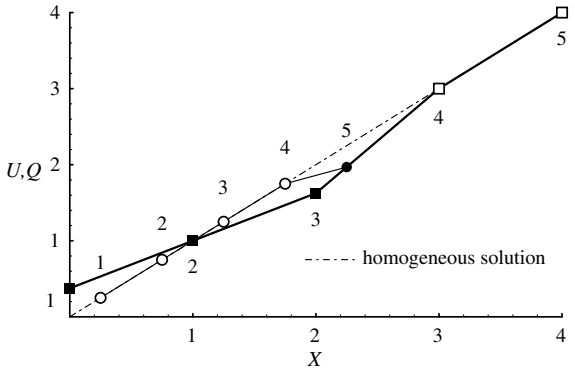

Fig. 6. Displacements of a coupled system using a diagonal approximation in the L_2 projection. Free nodes, projected nodes, free atoms and ghost atoms are shown, respectively, as □, ■, ○ and ●. Atom and element numbers are given within the figure by the digit shown above or below, respectively, the corresponding part.

case showed that no diagonal matrix could reproduce the homogeneous strain field exactly, as is required for the development of the Cauchy–Born correction in Section 5. These results enable us to conclude that use of diagonalized $\mathbf{M}_{\hat{U}\hat{U}}$ is not recommended. Either the original, L_2 projection method or the MLS alternative should be used.

We also examine a one-dimensional atomic chain with atoms subject to multiple neighbor interactions. For this example, we use the Lennard-Jones potential [31,32] that has been truncated [33] to a fifth nearest neighbor interaction. In this simulation, the chain has been given free boundary conditions on the atoms at either end and the system has been relaxed using a conjugate gradient, energy minimization algorithm. Fig. 7 shows the bond density correction calculated for each of the five different bond types. For clarity, the crystal itself is also shown with the same symbols as in Fig. 1 used for free and prescribed atoms and nodes. For the example shown, the four outer-most atoms on either end are free atoms while the remaining atoms are ghost atoms. In this example, it is clear how the volume $\tilde{\Omega}^{(a)}_{0(i)}$ differs with regard to each different bond type (i). It is also interesting to note that for this small system, ghost atoms are required within all elements in the interior due to the long range of the interatomic potential. Even within the center element $\rho_{(5)}$, the bond density correction associated with the bonds between an atom and its fifth nearest neighbors, never reaches the value of unity as ghost-free bonds are present. However, if the chain were made longer, we would see elements for which $\rho_{(i)} = 1$ for all 5 bond families, and ghost atoms could be omitted. In other words, the overlap region would essentially remain the same size that it is in Fig. 7 while more and more of the system can be modeled using pure continuum elements. Fig. 8 shows atomic displacements for two such longer one-dimensional atomic chains. In Fig. 8(a), the ratio of element size to atomic spacing is 2:1 and the system contains 26 atoms, 14 nodes and 13 elements. In Fig. 8(b), this ratio is 6:1 and the system contains 30 atoms, 6 nodes and 5 elements. In both figures, we see that without any free atoms on the surface, the system displays zero relaxation, and as successively more free atoms are used at the outer layers, the displacement field converges to that of a pure atomistic one-dimensional atomic chain. For the 2:1 ratio, this convergence occurs for 4 or more layers of free atoms while for the 6:1 ratio, it occurs for 6 layers of free atoms. Thus, the ratio of element size to atomic

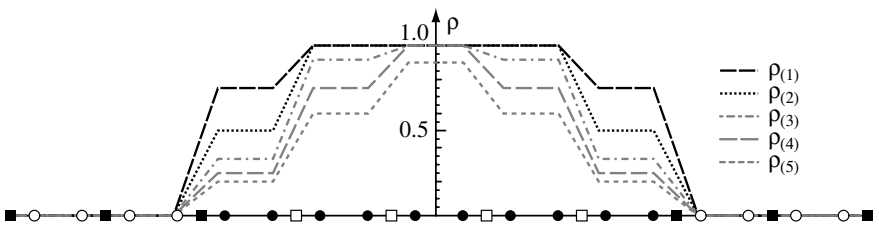

Fig. 7. $\rho_{(i)}(\mathbf{X})$ for a one-dimensional atomic chain using a fifth nearest neighbor Lennard-Jones potential. Free nodes, projected nodes, free atoms and ghost atoms are shown, respectively, as □, ■, ○ and ●.

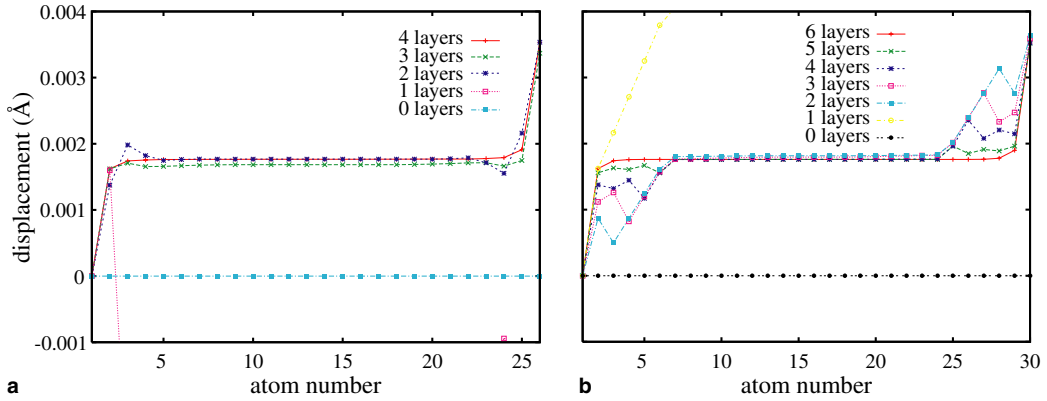

Fig. 8. Displacements for the relaxation of a free, one-dimensional atomic chain using a fifth nearest neighbor Lennard-Jones potential. Each curve represents a different number of layers of free atoms used at the chain's surfaces. The ratio of element size to atomic spacing is (a) 2:1 and (b) 6:1.

spacing, as well as the interaction range of the interatomic potential, affects how many layers of free atoms are needed to achieve this convergence.

7.2. Two-dimensional examples

We next examine the two-dimensional analog of the homogeneous deformation example given in the previous section. A rectangular region covered by a finite element mesh composed of four-node elements contains a limited region of atoms from a hexagonal crystal lattice, as shown in Fig. 9(a). These atoms interact through a nearest neighbor, quadratic potential. This region is homogeneously deformed by stretching the system's boundaries in the horizontal direction, as shown in Fig. 9(b). As mentioned in Section 6, this case proves to be unaffected by whether the cross terms in Eqs. (58) and (59) are included or not. For homogeneous deformation, the force coupling cross term between projected nodes and free atoms disappears,

$$\mathbf{R}_{\hat{\mathbf{U}}} = 0 \rightarrow \mathbf{R}_{\mathbf{Q}} = \frac{\partial \Pi_{\mathbf{Q}}}{\partial \mathbf{Q}} - \mathbf{F}_{\mathbf{Q}} = 0. \tag{119}$$

This decouples the displacement of the atoms from the displacement of the overlaying finite element mesh. Indeed, the correct displacement field for the free nodes is obtained if one assumes

$$\mathbf{R}_{\hat{\mathbf{Q}}} = 0 \rightarrow \mathbf{R}_{\mathbf{U}} = \left.\frac{\partial \Pi_{\mathbf{U}}}{\partial \mathbf{U}}\right|_{\rho=1} - \mathbf{F}_{\mathbf{U}} = 0. \tag{120}$$

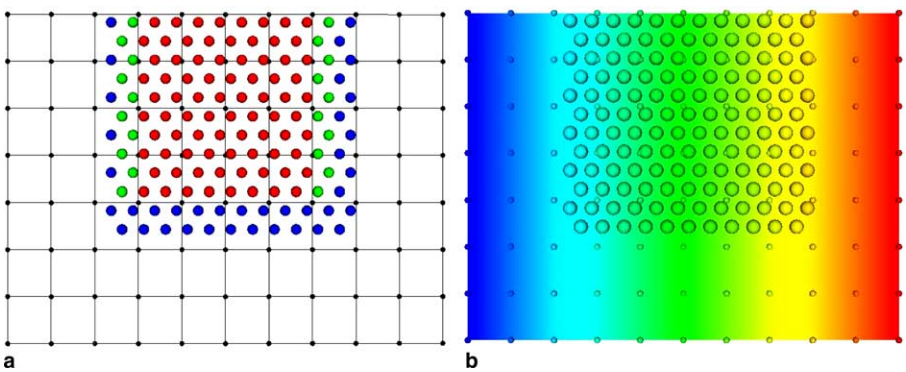

Fig. 9. (a) The two-dimensional coupled system consisting of a rectangular mesh of quadrilateral elements and a portion of a hexagonal lattice. Atoms are colored according to whether they are free (red) or ghost (green and blue). (b) The two-dimensional system homogeneously stretched in the horizontal direction. Color denotes the magnitude of stretch from zero (blue) to the highest value (red). (For interpretation of the references to color in this figure legend, the reader is referred to the web version of this article.)

In other words, the correct solutions for both the atomic and nodal displacement fields are obtained by treating them as separate problems. Their only connection is to use the Cauchy–Born rule to create the same material properties for the continuum as for the atomistic system, and the kinematic coupling used for interpolation and projection. Once again, it is important to realize that (120) results from eliminating the cross terms to calculate forces on free nodes due to ghost atoms and by setting bond densities, $\{\rho_{(i)}\}$, to unity. Only by omitting both coupling mechanisms is the correct FE solution realized. In addition, this decoupling of the problem is possible because the interatomic potential used is a nearest neighbor interaction only. Thus, the atomic crystal shown in Fig. 9 exhibits no surface relaxation and the Cauchy–Born model based on the same interatomic potential displays the same response as the actual crystal. For longer-ranged potentials, surface relaxation would occur and the deformations of the decoupled atomistic and continuum systems would no longer coincide.

A case for which the cross terms are important, and the correction for energy of overlapping elements is required to obtain the correct displacement solution, is one in which inhomogeneous deformation occurs, such as the relaxation of a crystal with free surfaces. Fig. 10(a) shows a system composed of a hexagonal lattice with free surfaces overlapped by a quadrilateral mesh. For the coupled system, the atoms that lie within the outer layer of elements are free atoms while all other elements contain ghost atoms. For this example, our potential is the Lennard-Jones potential [31,32] that has been shifted and truncated [33] such that an atom that interacts with all of its neighbors out to the 3rd nearest neighbor is equivalent to an atom within a bulk crystal. The system relaxes outward as shown in Fig. 10(b). The coupled system (red atoms) can be directly compared with a system simulated purely with atomistics (green atoms). Agreement is very good, but not perfect due to the severe inhomogeneous deformation at the corners.

In general, a minimum coverage of ghost atoms should be used as only ghost atoms that are within the interaction range (for the choice of interatomic potential) of free atoms are necessary. While the examples shown in this paper contain all atoms for all analyses, this was done strictly for illustration purposes to allow easy comparison of the coupled results with purely atomistic calculations. It is important to realize that presence of extraneous ghost atoms was not required to obtain a solution. Although excess computational work is done from interpolation of the coarse scale displacement field to these atoms, the cost of calculating the bond density corrections does not increase.

This two-dimensional surface relaxation problem also enables us to investigate the influence of the overlapping mesh on the coupled solution. Specifically, we examine a system in which triangular elements are used instead of quadrilateral ones. The mesh for this system is shown in Fig. 11(a). We notice that this system contains fewer atoms per element (202 atoms overlapped by 52 elements) as compared with the quadrilateral mesh (202 atoms overlapped by 25 elements). Fig. 11(b) shows the relaxed system with displacements magnified by a factor of 200 for both the coupled (red atoms) and purely atomistic (green atoms) systems. For this case, the displacement fields do not agree as well as for the quadrilateral mesh. One reason for the deficiency of the triangular mesh system is that while quadrilateral elements use four integration points per element for the FE calculation, triangular elements only use one point per element. The use of a single integration point reduces the spatial discretization of $\{\rho_{(i)}\}$ and results in a lower resolution representation of the coarse scale

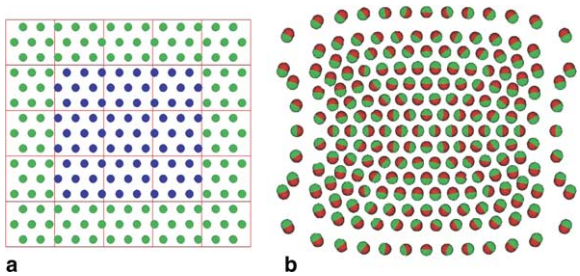

Fig. 10. (a) A two-dimensional, hexagonal lattice with free surfaces composed of free (green) and ghost (blue) atoms. The overlapping quadrilateral mesh is shown in red. (b) The relaxed configuration of (a) for the coupled system (red) and a system treated purely with atomistics (green). Displacements are magnified by a factor of 200. (For interpretation of the references to color in this figure legend, the reader is referred to the web version of this article.)

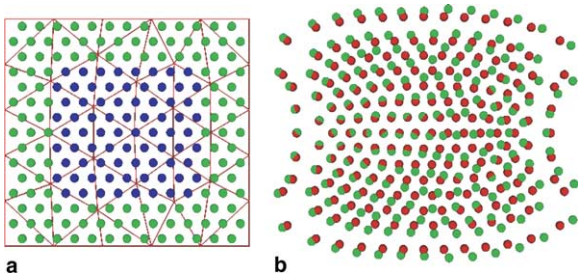

Fig. 11. (a) A two-dimensional, hexagonal lattice with free surfaces composed of free (green) and ghost (blue) atoms. The overlapping triangular FE mesh is shown in red. (b) The relaxed configuration of (a) for the coupled system (red) and a system treated purely with atomistics (green). Displacements are magnified by a factor of 200. (For interpretation of the references to color in this figure legend, the reader is referred to the web version of this article.)

portion of the solution. Also, triangular elements can only represent strains that are constant over the element. These factors lead to a loss of accuracy in the calculation of continuum field variables, and produce a stiffer overall response for the element.

7.3. Three-dimensional examples

A similar surface relaxation simulation is performed for the three-dimensional system composed of a cube of atoms. This cube contains a face-centered-cubic crystal of 32,000 atoms, and atoms interact with a fifth nearest neighbor Lennard-Jones potential with parameters suitable for the simulation of gold. This potential is given by the expression

$$\varphi(r^{\alpha\beta}) = \varphi_{\mathrm{LJ}}(r^{\alpha\beta}) - \varphi_{\mathrm{LJ}}(r^c) - [r^{\alpha\beta} - r^c]\varphi'_{\mathrm{LJ}}(r^c), \tag{121}$$

where

$$\varphi_{\mathrm{LJ}}(r) = 4\epsilon\left[\left(\frac{\sigma}{r}\right)^{12} - \left(\frac{\sigma}{r}\right)^{6}\right], \tag{122}$$

$r^{\alpha\beta} = |\mathbf{x}^{(\alpha)} - \mathbf{x}^{(\beta)}|$, $\epsilon = 0.567895$ eV, $\sigma = 2.623117$ Å and $r^c = 2.63\sigma$. Magnified displacements for half of the cube are shown in Figs. 12(a)–(c) for the purely atomistic system, coupled atomistic–continuum systems with hexahedral elements, and coupled system with tetrahedral elements, respectively. The ratio of element size to atomic spacing is approximately the same for calculations using the hexahedral (5.34:1) and tetrahedral (5.33:1) elements. In Fig. 12, atoms are colored according to their potential energy with red denoting the highest value for all atoms and blue denoting the lowest value. In Fig. 12(a), the highest potential energy atoms are found at the cube corners (colored red) and along the cube edges (colored yellow). The interior atoms possess the bulk potential energy of gold atoms, −3.93 eV, and are colored dark blue. In Fig. 12(b), interior ghost

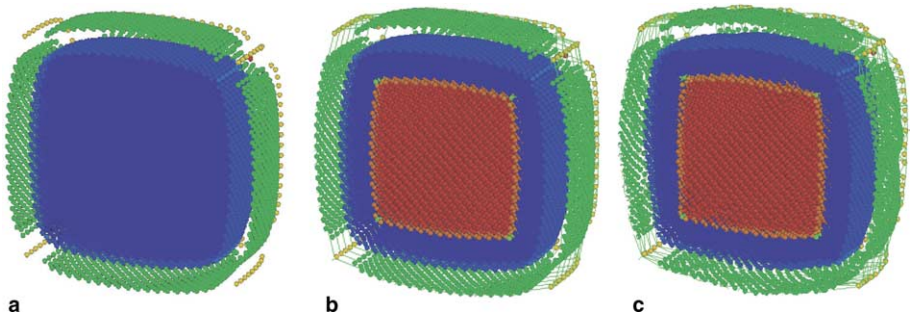

Fig. 12. One-half of a cube modeled with (a) pure atomistics, (b) coupled atomistics–continuum using a hexahedral element mesh, and (c) coupled atomistics–continuum using a tetrahedral element mesh. Displacements are magnified by a factor of 200.

atoms are also colored red and dark orange as they do not have any potential energy attributed to them unless bonded to free atoms in the outer layers. It is still observed that free atoms sufficiently far from the surface have potential energies equal to the bulk cohesive energy for gold, and that surface, edge and corner atoms have higher potential energies. Comparison of potential energies for the free atoms in the coupled system with the same respective atoms in the purely atomistic system shows agreement to the fourth significant figure. Atomic potential energy is dominated by the creation of surfaces, while a change in energy due to relaxation is a secondary effect.

Fig. 12(c) shows similar values of energies to those found in Fig. 12(b), again agreeing with the purely atomistic system's energies to the fourth significant figure. However, the relaxed configuration with the tetrahedral mesh does not display the same level of accuracy as with the hexahedral mesh. Once again, this loss of accuracy is due to the hexahedral elements possessing the ability to represent varying strain while the tetrahedral elements have only a single integration point at which the bond density is determined and can only represent constant strain.

Further comparison between the purely atomistic and coupled systems can be made through examination of the stress field created by the surface relaxation. Fig. 13 shows the variation of the hydrostatic stress for nodes along a line passing through the middle of the cube between opposing faces. The different curves correspond with the numbers of surface layers of free atoms, with 20 layers corresponding to the purely atomistic system. It is observed that when 6 or more atomic layers are used within the atomic region, the coupled system essentially matches the stress field obtained with pure atomistics, especially with regard to the value of tensile stress within the outer layers of the cube. The interior compressive stress also agrees very well, especially for the use of 6 or 8 atomic layers. For comparison, we can also examine the same hydrostatic stress curves produced for system coupled only through kinematics. For these analyses, neither the cross terms nor the bond density corrections to the Cauchy–Born rule are used. As shown in Fig. 14, we observe that the interior compressive stress agrees best when using 6 or 8 atomic layers and overall, agreement is not as good as when force coupling mechanisms are implemented. This is made obvious by the much wider range of values of compressive stress for the nodes within the cube.

7.4. Analysis of computational cost

The numerical examples in Sections 7.1–7.3 are selected to highlight the basic characteristics of the coupling approach. As such, they are too small to provide a representative demonstration of the computational efficiency of the method. In particular, they have a much larger atomistic region compared with the continuum region than we would expect in typical applications of coupled analysis. Also, the region of "overlap" is large compared to the total size of the computational domain. Finally, the ratio of the element dimension to the

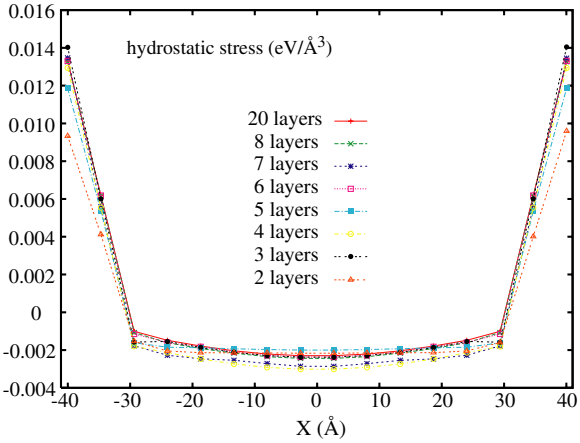

Fig. 13. Hydrostatic stress for nodes along a line passing through the middle of the relaxed cube. The legend refers to the number of layers of free atoms used for the outer surface of the crystal.

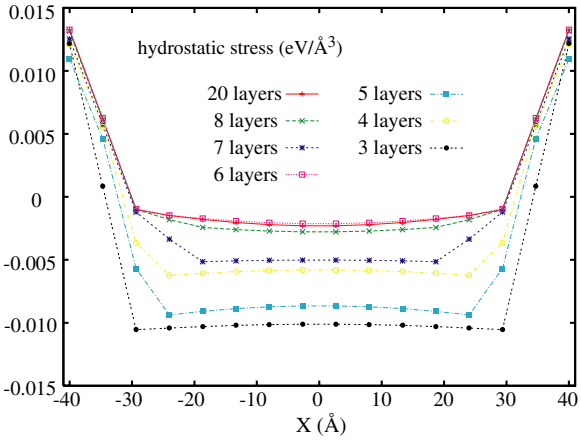

Fig. 14. The same curves as in Fig. 13 for a system coupled only through kinematics and use of the Cauchy–Born rule (no force coupling mechanisms used).

bond length is smaller than would be optimal for a large scale calculations, and generally, the element size would be nonuniform, increasing with distance from the atomistic regions.

Nevertheless, we use the three-dimensional example presented in Section 7.3 to provide some illustration of the computational cost of the coupled approach. The crystal contains a total of $n_{\text{total}}^{\text{atom}} = 32{,}000$ atoms. For the coarse scale problem, we discretize the cubic domain into $n_{\text{total}}^{\text{element}} = 15^3 = 3375$ hexahedral elements, for an average of 9.5 atoms per element. The coarse scale problem is solved with a total Lagrangian, finite deformation element formulation using eight integration points per element. Since the cost of computing the integration point stress using the Cauchy–Born rule is comparable to the cost of computing the total force on an atom, we would generally select the element dimension so that the number of atoms replaced with elements would be substantially greater than the number of integration points.

We use the time required for a single evaluation of the total force acting on the atoms and nodes in the system for a detailed analysis of the computational cost of the coupled approach. For both quasistatic and dynamic analyses, the repeated evaluation of the system force will comprise the majority of the computational cost. Using the moving least square projection of atomistic information onto the coarse scale described in Section 4, the force acting on the atoms and nodes is given by (58) and (59), respectively. Recall that in these expressions, $\frac{\partial \Pi_{\mathbf{Q}}}{\partial \mathbf{Q}}$ represents the force on atoms due to atomic bonds, $\frac{\partial \Pi_{\mathbf{U}}}{\partial \mathbf{U}}$ represents the finite element-derived, coarse scale forces on the nodes, and all other contributions to the forces, aside from the externally applied forces $\mathbf{F}_{\mathbf{Q}}$ and $\mathbf{F}_{\mathbf{U}}$, are due to coupling. Forces on ghost atoms $\frac{\partial \Pi_{\mathbf{Q}}}{\partial \mathbf{Q}}$ and projected nodes $\frac{\partial \Pi_{\mathbf{U}}}{\partial \mathbf{U}}$ are computed together with and as part of the forces acting on free atoms and nodes. Therefore, the cost of these terms is difficult to isolate and is instead included with the cost of the atomistic and coarse scale computations, respectively. The costs that can be associated strictly with the coupling terms are limited to the product of force vectors with the shape function matrices given in (58) and (59).

Fig. 15 shows how the contributions to the computational cost for each evaluation of the system force change with the number of atomistic layers in the crystal. The number of layers is counted from the surface inward, reaching 20 layers when the entire domain is represented atomistically. The times are normalized by $t_{\text{F}}^{\text{atom}}$, the time required for a single evaluation of the force in a purely atomistic calculation. Comparing a purely atomistic calculation to a purely finite element calculation over the entire domain, we find that on a per volume basis the ratio of the costs for a single evaluation in the finite element and atomistic forces is $t_{\text{F}}^{\text{coarse}}/t_{\text{F}}^{\text{atom}} = 0.80$, which is comparable to but slightly better than the 0.84 ratio of integration points to atoms per unit volume. Curves (1)–(3) show the computational time for a single evaluation of the atomistic, coarse scale, and coupling terms in the system force, respectively. The total time is shown by curve (4). As we would expect, the cost of the atomistic part of the calculation increases with more atomic layers, while the cost of the coarse scale calculation decreases. The cost of the coupling terms stays relatively small, decreasing from approximately 3% to 2% of $t_{\text{F}}^{\text{atom}}$ as the number of atomic layers decreases from 20 to 2. Since atomistic layers

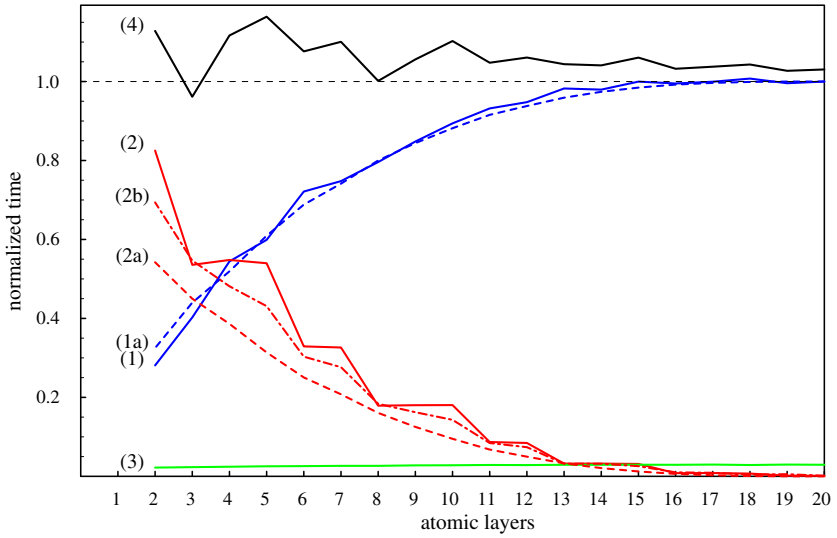

Fig. 15. Variation in the computational time with the number of atomic layers for the 3D cube relaxation simulation from Section 7.3, showing the time for the (1) atomistic, (2) coarse scale, and (3) coupling terms in the system force calculation, as well as (4) the total time. All times are normalized by $t_{\mathrm{F}}^{\mathrm{atom}}$, the cost of evaluating the force in a purely atomistic calculation (20 layers). Also shown is (1a) the time $t_{\mathrm{F}}^{\mathrm{atom}}$ scaled relative numbers of atoms, (2b) the normalized, projected cost of the coarse scale computation, and (2c) the normalized, projected cost of the coarse scale computation adjusted for thickness of the overlap layer.

are replaced with coarse scale calculations that for the given element dimensions have approximately the same cost per volume, the total cost for each evaluation of the force does not change dramatically with differing numbers of atomistic layers.

Curves (1a), (2a), and (2b) in Fig. 15 demonstrate how we would expect the computational cost to vary based on a per volume scaling of the purely atomistic and purely finite element calculations. Curve (1a) is the time $t_{\mathrm{F}}^{\mathrm{atom}}$ for a single evaluation of the force in a purely atomistic calculation scaled by the relative number of free atoms in the coupled system $n^{\mathrm{atom}}/n_{\mathrm{total}}^{\mathrm{atom}}$. Comparing curves (1) and (1a), the cost of this part of the calculation scales clearly with the number of free atoms, and there is little effect associated with calculation of forces on ghost atoms. Curve (2a) is the time $t_{\mathrm{F}}^{\mathrm{coarse}}$ for the purely finite element calculation scaled by the volume fraction of the system not represented with atoms $1 - n^{\mathrm{atom}}/n_{\mathrm{total}}^{\mathrm{atom}}$. Comparing curves (2) and (2a), we do see that the coarse scale part of the coupled calculation displays additional costs associated with the overlap region. Curve (2) also displays a higher degree of nonsmoothness compared with curve (1). The calculations with 3, 6, 8, and 11 layers appear more efficient than those with 2, 5, 7, and 10 layers. Curve (2b) is constructed by scaling the difference between curves (2) and (2a) by the relative thickness of the overlap layer. Because the geometry used for this calculation does not produce a simple planar boundary between the atomistic and continuum regions, a measure of the effective thickness of the overlap is calculated from the volume of the overlap layer, determined from the number of elements in the overlap, and its effective area, determined from the surface area of the cube separating the free and ghost atoms. Comparing curves (2a) and (2b) reveals that the reduced efficiency is associated with additional thickness of the overlap region. As curve (2a) shows, the thickness varies depending on where the crystal is terminated with respect to the element boundaries. With 3 atomic layers, the outer most layer of elements in the cube is completely filled with free atoms, and the ghost atoms are contained only in the second layer of elements from the surface. This configuration yields 866 elements in the overlap region. Using just 2 atomic layers, the interaction range of the atomistic potential dictates that the outer *two* layers of elements contain ghost atoms, meaning 2040 of the 3375 elements in the mesh participate in the overlap.

There are additional costs associated with coupled simulations beyond the force calculation described in Fig. 15. The most significant among these is determination of the bond densities in the overlap layer, which involves minimization of a bound constrained problem for a system that is otherwise linear in the unknowns.

These densities need to be determined only once for a given overlap configuration. The formulation requires determination of the density for each bond family at each integration point of elements in the overlap layer. The fifth neighbor potential used for the example in Section 7.3 has 39 bond families. Developing efficient methods for solving these densities is a topic of our future work. There are also costs associated with initializing the projection and interpolation operations. This involves mapping the atomic positions into elements in the mesh, determining domains of influence for the moving least squares fits, and calculation of the meshless shape functions. As with the bond densities, these quantities need to be determined only once for a given overlap configuration. In our example calculations, the cost of this initialization ranges from approximately 3 to 18 $t_{\mathrm{F}}^{\mathrm{atom}}$ as the number of atomic layers increases from 2 to 20.

In this section, we present an analysis of the computational cost using a configuration for which the atomistic and coarse scale calculations have approximately the same cost on a per volume basis. Generally, the reduction in cost achieved by using a coarse scale representation of an atomistic crystal scales as $(h/a_0)^3$, where h is the element dimension and a_0 is the lattice parameter, which quickly becomes dramatic as the element dimension increases. Our results indicate that for a larger system in which the atomistic region comprises just a small fraction of the total system volume, the cost of computing the coupling contributions to the system force will be small compared with the significant saving in computational cost gained by reducing the number of atoms in the system.

8. Summary

We have presented a formulation for an atomistic-to-finite element coupling method comprised of three components:

- Kinematics – the description of how displacements are transferred from nodes and atoms in $\mathscr{N}$ and $\mathscr{A}$ to nodes and atoms in $\hat{\mathscr{N}}$ and $\hat{\mathscr{A}}$.
- Coupled equilibrium equations – equations derived from the total energy of the coupled system incorporating the kinematics of the coupling in displacements.
- Generalized Cauchy–Born – modifications to the usual Cauchy–Born rule needed to compensate for regions of overlap between the continuum and the underlying lattice.

The moving least squares field construction, like that provided by RKPM, appears the most promising for the projection of atomistic displacements to the nodes in $\hat{\mathscr{N}}$. The formulation provides a method for "fitting" a displacement field over atoms in a given region that can be constructed to reproduce a selected order of polynomials exactly. This property can be used to guarantee that a homogeneous deformation field is transferred to the nodes exactly. Moreover, RKPM has well-defined spectral properties, especially when calculated over a regular set of points, such as a lattice. These properties will allow us to characterize exactly which scale or wavelength of information is transferred to the finite element nodes and which ones need to be accommodated in some other fashion.

The most significant outcome of this work has been the development of a generalized Cauchy–Born procedure for use in finite elements with a limited amount of underlying crystal lattice. The method does suggest it should yield better performance with mesh refinement. The improved results would be the result not only of the finer scale in the finite element basis function, but also as a result of higher resolution in the discretized bond density function. Note that this function only needs to be determined once, over the undeformed configuration, for a given system geometry.

We do observe that the approach described in this paper, specifically the inclusion of force cross terms within the equilibrium equations and the bond density corrections to the Cauchy–Born rule, does possess good stability with regard to yielding a numerical solution. Omission of these features often results in energy minimization algorithms failing to converge to any solution for many of the systems described in this paper. This failure is highly dependent on the orientation of the mesh with respect to the underlying atomic lattice and the size of lattice region used. Under limited conditions and when considering only nearest-neighbor interactions, the issue of overlap correction can be addressed by terminating the atomistic crystal in specific ways within the mesh. This approach has allowed previous efforts in atomistic–continuum coupling to produce accurate

results. Our development and inclusion of these features eliminates this dependency, and is more generalized for the proper treatment of multi-dimensional systems and longer range potentials.

A remaining concern with this approach, to be addressed in future work, regards the quantification of solution errors obtained with coupled systems. We have minimized the error through our use of cross terms within the equilibrium equations and the bond density corrections to the Cauchy–Born rule. However, several approximations are made to obtain solutions for those same bond density corrections, including the use of a limited number of integration points at which the bond densities $\rho_{(i)}$ are evaluated. Whether the error these approximations introduce to our solution is much smaller than error eliminated by our approach remains an unanswered question.

Rigorous testing of the approach presented in this paper is also warranted to assess its performance when applied to materials simulations ubiquitous to the field of coupled simulations. Examples of such simulations include crack growth [7,13,34] and nanoindentation [35–37] in both brittle [7,13,36] and ductile [34,35,37] materials. Our method would be useful for the analysis of nano-scale wires and films and polycrystalline materials. For these types of systems, the regions interior to either free surfaces or grain boundaries would be modeled with finite elements while the regions near the structural inhomogeneities would be modeled with atoms. The overlap region should not intersect either grain boundaries or other crystal defects as the energy of any such defect would be artificially minimized by the bond density correction calculations. Also, this method does require that any continuum region enclosed by atomistic boundaries possess a single crystal orientation, while disconnected continuum regions may differ in this orientation. Proper use of our coupled method for these systems would enable treatment of geometries with dimensions up to several hundred nanometers and even the micron range.

Several areas for further development of our approach have been identified. Currently, we are working to parallelize the algorithms discussed in this paper for application to large systems. We also plan to apply the approach for solving the bond density corrections to multi-body types of interatomic potentials such as the embedded atom method [38], used for modeling FCC and BCC crystals, and the Stillinger–Weber potential [39], used for modeling silicon and other materials with the diamond cubic crystal structure. Finally, the methodology presented in this paper will be adapted to analyze coupled dynamic systems. The bond density corrections developed here will still be used to compute the potential energy portion of the system's Hamiltonian, but more thought will be required with regard to the partitioning and calculation of the kinetic energy portion.

Acknowledgments

The authors gratefully acknowledge input provided by discussions with Gregory J. Wagner, Reese E. Jones, Christopher J. Kimmer, Jeffrey J. Hoyt, Edmund B. Webb III and Sylvie Aubry of Sandia National Laboratories. Sandia is a multiprogram laboratory operated by Sandia Corporation, a Lockheed Martin Company, for the United States Department of Energy's National Nuclear Security Administration under contract DE-AC04-94AL85000.

References

[1] Materials research by means of multiscale computer simulation, Bulletin, Materials Research Society, March, 2001.
[2] J. Fish, Z. Yuan, Multiscale enrichment based on partition of unity, International Journal of Numerical Methods in Engineering 62 (10) (2005) 1341–1359.
[3] S. Kohlhoff, S. Schmauder, A new method for coupled elastic-atomistic modelling, in: V. Vitek, D.J. Srolovitz (Eds.), Atomistic Simulation of Materials: Beyond Pair Potentials, Plenum Press, New York, 1989, pp. 411–418.
[4] S. Kohlhoff, P. Gumbsch, H.F. Fischmeister, Crack propagation in BCC crystals studied with a combined finite-element and atomistic model, Philosophical Magazine A 64 (1991) 851–878.
[5] E.B. Tadmor, M. Ortiz, R. Phillips, Quasicontinuum analysis of defects in solids, Philosophical Magazine A 73 (6) (1996) 1529–1563.
[6] R.E. Rudd, J.Q. Broughton, Coarse-grained molecular dynamics and the atomic limit of finite elements, Physical Review B 58 (1998) R5893–R5896.
[7] J.Q. Broughton, F.F. Abraham, N. Bernstein, E. Kaxiras, Concurrent coupling of length scales: methodology and application, Physical Review B 60 (1999) 2391–2403.
[8] G.J. Wagner, W.K. Liu, Coupling of atomistic and continuum simulations using a bridging scale decomposition, Journal of Computational Physics 190 (2003) 249–274.

[9] L.E. Malvern, Introduction to the Mechanics of a Continuous Medium, Wiley, New York, 1969.
[10] K. Huang, On the atomic theory of elasticity, Proceedings of the Royal Society of London A 203 (1950) 178–194.
[11] M. Born, K. Huang, Dynamical Theories of Crystal Lattices, Clarendon Press, Oxford, 1956.
[12] R.E. Rudd, Coarse-grained molecular dynamics: dissipation due to internal modes, in: Thin Films: Stresses and Mechanical Properties IXMaterials Research Society Symposium Proceedings, vol. 695, Materials Research Society, 2002, pp. 499–504.
[13] H.S. Park, E.G. Karpov, W.K. Liu, P.A. Klein, The bridging scale for two-dimensional atomistic/continuum coupling, Philosophical Magazine 85 (1) (2005) 79–113.
[14] H.S. Park, E.G. Karpov, P.A. Klein, W.K. Liu, Three-dimensional bridging scale analysis of dynamic fracture, Journal of Computational Physics 207 (2) (2005) 588–609.
[15] S.P. Xiao, T. Belytschko, A bridging domain method for coupling continua with molecular dynamics, Computer Methods in Applied Mechanics and Engineering 193 (2004) 1645–1669.
[16] W.A. Curtin, R.A. Miller, Atomistic/continuum coupling in computational materials science, Modelling and Simulation in Materials Science and Engineering 11 (2003) R33–R68.
[17] V.B. Shenoy, R. Miller, E.B. Tadmor, D. Rodney, R. Phillips, M. Ortiz, An adaptive finite element approach to atomic-scale mechanics – the quasicontinuum method, Journal of the Mechanics and Physics of Solids 47 (1999) 611–642.
[18] J. Knap, M. Ortiz, An analysis of the quasicontinuum method, Journal of the Mechanics and Physics of Solids 49 (2001) 1899–1923.
[19] I. Stakgold, The Cauchy relations in a molecular theory of elasticity, Quarterly of Applied Mechanics 8 (1950) 169–186.
[20] E.B. Tadmor, G.S. Smith, N. Bernstein, E. Kaxiras, Mixed finite element and atomistic formulation for complex crystals, Physical Review B 59 (1) (1999) 235–245.
[21] P. Zhang, Y. Huang, P.H. Geubelle, P.A. Klein, K.C. Hwang, The elastic modulus of single-wall carbon nanotubes: a continuum analysis incorporating interatomic potentials, International Journal of Solids and Structures 39 (2002) 3893–3906.
[22] T.J.R. Hughes, The Finite Element Method: Linear Static and Dynamic Finite Element Analysis, Prentice-Hall, Englewood Cliffs, NJ, 1987.
[23] J.R. Shewchuk, An introduction to the conjugate gradient method without the agonizing pain (1994). Available from: <http://www.cs.cmu.edu/~quake-papers/painless-conjugate-gradient.pdf>.
[24] W.K. Liu, Y. Chen, S. Jun, J.S. Chen, T. Belytschko, C. Pan, R.A. Uras, C.T. Chang, Overview and applications of the reproducing kernel particle methods, Archives of Computational Methods in Engineering: State of the Art Reviews 3 (1996) 3–80.
[25] W.K. Liu, Y. Chen, Reproducing kernel particle methods, International Journal for Numerical Methods in Fluids 20 (1995) 1081–1106.
[26] H. Gao, P. Klein, Numerical simulation of crack growth in an isotropic solid with randomized internal cohesive bonds, Journal of the Mechanics and Physics of Solids 46 (2) (1998) 187–218.
[27] P. Klein, H. Gao, Crack nucleation and growth as strain localization in a virtual-bond continuum, Engineering Fracture Mechanics 61 (1998) 21–48.
[28] H. Engl, M. Hanke, A. Neubauer, Regularization of Inverse Problems, Kluwer Academic Publishers, Dordrecht, 1996.
[29] Tahoe, Sandia National Laboratories, 2004. Available from: <http://tahoe.ca.sandia.gov>.
[30] E. Hinton, T. Rock, O.C. Zienkiewicz, A note on mass lumping and related processes in the finite element method, Earthquake Engineering and Structural Dynamics 4 (1976) 245–249.
[31] J.E. Lennard-Jones, The determination of molecular fields I. From the variation of the viscosity of a gas with temperature, Proceedings of the Royal Society of London A 106 (1924) 441.
[32] J.E. Lennard-Jones, The determination of molecular fields II. From the equation of state of a gas, Proceedings of the Royal Society of London A 106 (1924) 463.
[33] J.M. Haile, Molecular Dynamics Simulation Elementary Methods, Wiley, New York, 1992.
[34] R. Miller, E.B. Tadmor, R. Phillips, M. Ortiz, Quasicontinuum simulation of fracture at the atomic scale, Modelling and Simulation in Materials Science and Engineering 6 (1998) 607–638.
[35] E.B. Tadmor, R. Miller, R. Phillips, M. Ortiz, Nanoindentation and incipient plasticity, Journal of Materials Research 14 (6) (1999) 2233–2250.
[36] G.S. Smith, E.B. Tadmor, N. Bernstein, E. Kaxiras, Multiscale simulations of silicon nanoindentation, Acta Materialia 49 (2001) 4089–4101.
[37] J. Knap, M. Ortiz, Effect of indenter-radius size on Au(0 0 1) nanoindentation, Physical Review Letters 90 (22) (2003) 226102.
[38] S.M. Foiles, M.I. Baskes, M.S. Daw, Embedded-atom-method functions for the fcc metals cu, ag, au, ni, pd, pt, and their alloys, Physical Review B 33 (1986) 7983–7991.
[39] F.H. Stillinger, T.A. Weber, Computer simulation of local order in condensed phases of silicon, Physical Review B 31 (1985) 5262–5271.